International Journal of Plasticity 183 (2024) 104158

Contents lists available at ScienceDirect

International Journal of Plasticity

journal homepage: www.elsevier.com/locate/ijplas

A generalized, computationally versatile plasticity model framework - Part II: Theory and verification focusing on shear anisotropy

Yong Hou [a,*], Junying Min [b], Hyung-Rim Lee [c], Jinjin Ha [d], Namsu Park [e,*], Myoung-Gyu Lee [c]

[a] Institute of Forming Technology and Lightweight Components (IUL), TU Dortmund University, Dortmund 44227, Germany
[b] School of Mechanical Engineering, Tongji University, Shanghai 201804, China
[c] Department of Materials Science and Engineering & RIAM, Seoul National University, Seoul 08826, South Korea
[d] Department of Mechanical Engineering, University of New Hampshire, Durham 03824, USA
[e] Flexible Manufacturing R&D Department, Korea Institute of Industrial Technology, Incheon 21999, South Korea

ARTICLE INFO

Keywords:
Plastic anisotropy
Stress triaxiality-dependent general framework
Shear deformation
Yield criterion
Anisotropic hardening
Non-associated flow rule

ABSTRACT

Shear-dominated deformation (SHDD) is pivotal in sheet metal forming; however, comprehensive modeling of plastic anisotropy in SHDD, specifically shear anisotropy considering both yield stress and plastic flow, has been inadequately addressed in existing literature. In this work, a generalized constitutive framework is introduced on the basis of stress triaxiality-dependent state variable to accurately emulate plastic anisotropy and the physics-based shear constraint in SHDD. The framework is capable to seamlessly integrate with existing yield criteria, preserving computational efficiency and versatility. Notably, the yield function, anisotropic parameters, and their optimization or analytical determination for the non-shear deformation state remain unaltered. When integrated with the Hill48 yield function, featuring either one or two anisotropic parameters within the generalized constitutive framework, precise characterization of yield strength and plastic flow in SHDD is achieved. The applicability of the framework extends to various anisotropic yield functions such as the widely employed Yld2k-2d and the sixth-order polynomial (Poly6) function as a class of associated flow rule-based yield functions, and one non-quadratic yield function for non-associated flow rule scenarios. Experimental validation with two engineering sheet metals, high-strength dual-phase steel DP980 and high-strength aluminum alloy AA7075-T6, was conducted. Comparative analyses with several recently proposed yield criteria, especially Poly6–18p, highlighted the efficiency of the proposed constitutive framework. Furthermore, this study explores intrinsic shear constraints, particularly the absence of through-thickness strains under in-plane shear stress. Additionally, it offers an enhanced description of plastic anisotropy in shear yield stress within the general framework, providing valuable insights into the complexities of SHDD.

* Corresponding authors.
E-mail addresses: Yong.Hou@iul.tu-dortmund.de, yonghou.1019@gmail.com (Y. Hou), nspark@kitech.re.kr (N. Park).

https://doi.org/10.1016/j.ijplas.2024.104158
Received 4 June 2024; Received in revised form 9 October 2024;
Available online 28 October 2024

1. Introduction

Sheet metal often experiences complex stress states during advanced forming processes. The enhancement of accurate plasticity modeling not only improves high-fidelity finite element (FE) simulations but also contributes to the advancement of digital twin applications in industries such as automotive and aerospace. Moreover, the utility of high-precision plasticity models extends to generating substantial amounts of precise and representative virtual data, particularly beneficial for machine learning-based models.

Numerous phenomenological constitutive models have been proposed and employed to characterize the anisotropic behavior of metal sheets under complex loading conditions. Notable contributions in this field have been made by Hill and Barlat, as extensively documented in literature (Barlat et al., 2005, 1997, 2003; Barlat et al., 2011, 2013, 1991; Barlat et al., 2007, 2020; Hill, 1948, 1979, 1990). Additionally, several high-precision and high-flexibility anisotropic plasticity models have been introduced (Banabic et al., 2003; Hu et al., 2017b; Lou et al., 2013; Mu et al., 2024; Yoon et al., 2005, 2014; Yoshida et al., 2013). Over an extended period, the stress state-dependent damage and fracture behavior of metal sheets have been extensively investigated (Baral et al., 2024; Li et al., 2019; Mirnia and Vahdani, 2020; Shang et al., 2021; Shen et al., 2024; Zheng et al., 2023). However, recent attention has been directed towards the stress state dependency of plastic anisotropy in advanced sheet metals, as highlighted in recent studies (Fuhg et al., 2023; Hou et al., 2023b; Hu et al., 2023; Lou et al., 2022; Park et al., 2024). As elucidated by Brosius et al. (2018), complex stress states beyond simple uniaxial tension (UT), such as biaxial tension (BT), plane strain tension (PST), and simple shear (SH), are evident in forming processes like deep drawing of a cross-cup. Due to this, complex yield functions rather than Hill48 (Hill, 1948), which only uses data from the UT test, are used nowadays. Advanced yield functions such as Yld2k-2d (Barlat et al., 2003) based on the associated flow rule (AFR) are able to consider the UT and equi-biaxial tension (EBT) conditions. In the AFR, the plastic potential is assumed to be identical to the yield surface. Consequently, yield stresses and plastic flow directions are generally used simultaneously as inputs to optimize or determine the anisotropic parameters. The exponent of the yield function (Barlat et al., 2005; Hou et al., 2023c, 2020) or other yield surface shape parameters (Cazacu, 2018; Drucker, 1949; Hou et al., 2022b; Zhang and Lou, 2023; Zhou et al., 2023) are used to indirectly regulate the PST state. Hou et al. (2022a) proposed for the first time a new modeling approach of directly using the anisotropic yield stress pairs in the PST state along three loading directions (0°, 45° and 90° to the rolling direction (RD) of sheet metals) to analytically identify the anisotropic parameters. This modeling approach was applied to a fourth-order polynomial yield function under the non-associated flow rule (NAFR-Poly4). Note that for the PST state in Hou et al. (2022a) and this work, the minor stress component was assumed to be 0.5 of the major stress component. The NAFR effectively captures plastic anisotropy by employing distinct yield stress and plastic potential functions, offering greater versatility compared to the AFR. The anisotropic parameters in the yield stress function are typically calibrated using yield stresses, while the plastic potential function parameters are calibrated separately using plastic flow directions, such as *r*-values (Lankford coefficients). It should be noted that in the application of the NAFR, it is critical to avoid crossover between yield stress and *r*-value in parameter determination of yield stress function and plastic potential function. Failure to do so will result in physically inappropriate parameter calibration for either the yield stress function or the plastic potential function. Recently, Mu et al. (2024) developed a modified anisotropic Hill48 yield criterion that accounts for loading in any principal stress direction, accurately describing the continuous evolution of stresses under UT, EBT, and near PST conditions. Wu et al. (2024) introduced a distortional hardening model capable of capturing the three stress states (UT, PST, and SH) on the plastic work contours of TWIP980 steel.

Among various stress states, SH is the crucial one for sheet metal deformation (Brosius et al., 2018; Dick and Korkolis, 2015; Grolleau et al., 2022; Han et al., 2022, 2024; Hou et al., 2021; Meyer et al., 2020; Rousselier, 2022; Sato et al., 2023). It should be noted that this study focuses on simple shear deformation rather than pure shear when describing shear loading. Simple shear more accurately represents the conditions typically used in experimental characterization of sheet materials under shear loading. Additionally, at low strain levels (below 20%), pure shear and simple shear can be considered equivalent (Boogaard, 2002). Fig. 1 shows the 3D yield surface in the σ_{11}-σ_{22}-σ_{12} stress space (plane stress condition) and different stress states on the yield surface. The stress components of material under SH along different loading directions are also expressed in Fig. 1. Unlike other stress states, SH with a stress triaxiality of zero not only exhibits anisotropy but also symmetry: $\tau_0 = \tau_{90}$ and $\tau_{45} = \tau_{135}$. In addition, as stated by Abedini et al. (2018), many phenomenological yield functions may lead to non-physical artifacts in SH region. These non-physical artifacts manifest as non-zero hydrostatic stress or through-thickness strains generated under in-plane shear stress, which violate the fundamental definition of the shear loading condition. Fortunately, these artifacts were removed with a newly proposed shear calibration constraint, which was imposed on the Yld2k-2d yield function. Later, this additional shear calibration constraint was adopted by Zhang et al. (2022a) in their proposed plastic potential (anisotropic Drucker function) based on the NAFR to enforce the simulated shear stress at zero hydrostatic pressure.

Regarding the strength difference and plastic anisotropy of sheet metals in the shear-dominated deformation (SHDD), several plasticity models have been proposed. A yield function with four parameters was proposed by Bassani (1977) to approximate a wide range of transversely isotropic yield loci, considering the yield stresses under SH and EBT during calibration. The normalized third stress invariant (of an isotropic material) is identical for SH and PST. Hence, yield stresses under SH and PST loadings present a fixed positive linear relationship in the pressure-insensitive Hosford72 or Drucker49 yield functions (Hou et al., 2023b). To describe the strength difference among SH, PST and UT, Lou et al. (2020, 2022) considered the pressure effect in two isotropic stress-invariant-based NAFR yield functions. Barlat and Lian (1989) initially proposed using two yield stresses under SH along different loading directions, namely σ_{SH0} and σ_{SH45}, to calibrate the parameters of the well-known anisotropic non-quadratic Barlat-Lian89 yield function. Fig. 2 illustrates the predicted yield loci, yield stresses, and *r*-values of AA2090-T3 under UT using the Raemy yield criterion (Raemy et al., 2017, 2018) with varying numbers of coefficients. While the predictions in the first and third quadrants remain almost consistent across all variants, notable discrepancies arise in the predicted yield locus in SHDD. Therefore, calibrating the shape of the

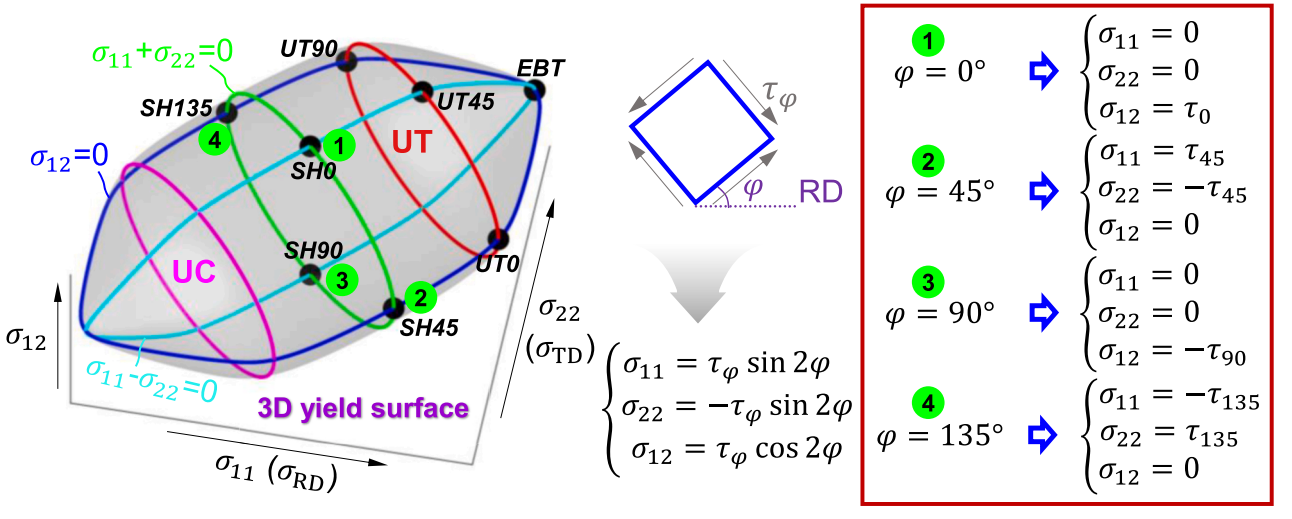

Fig. 1. 3D yield surface, various stress states, and derivation of SH deformation.

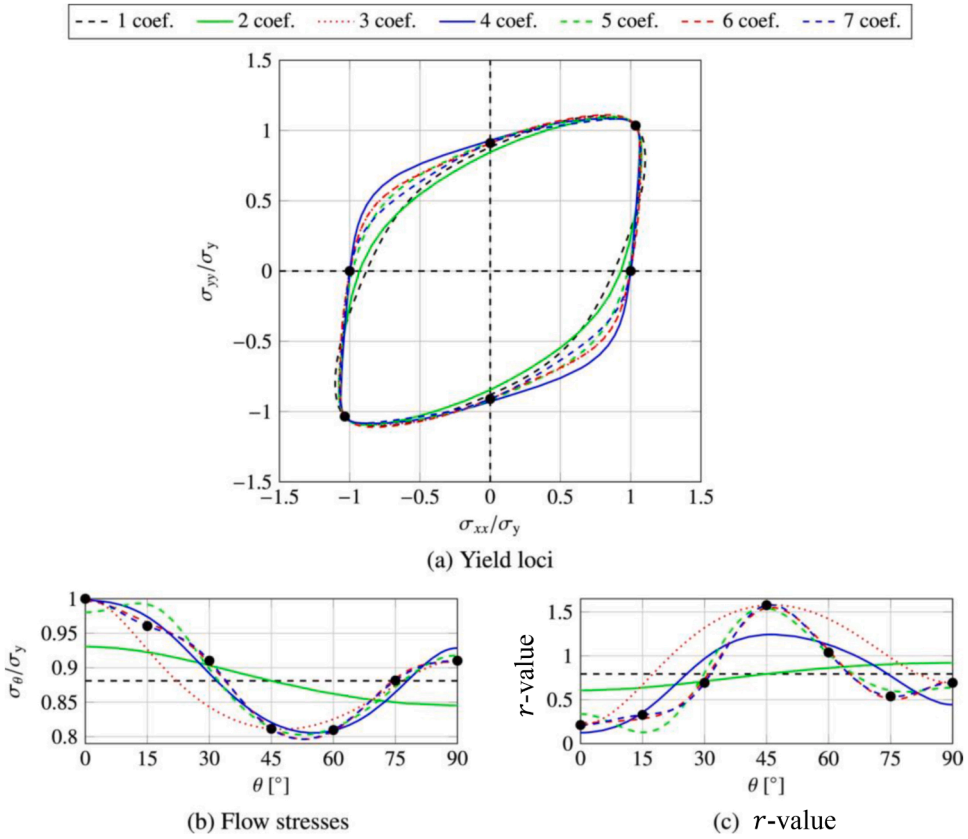

Fig. 2. Characterization of yield behavior using the Raemy2018 yield criterion (Raemy et al., 2018) employing a two-dimensional Fourier series with varying numbers of coefficients: (a) yield loci in the normal plane, (b) uniaxial flow stresses, and (c) r-values of AA2090-T3 (copyright).

yield locus in SHDD becomes imperative, particularly in advanced forming processes characterized by such deformation.

Several advanced anisotropic plasticity models incorporate the SH yield stresses during the calibration step. Hu et al. (2021) proposed an analytical method to determine 16 anisotropic parameters with one yield stress under SH for a sixth-order polynomial (Poly6) yield function. He et al. (2022) introduced an enhanced version of the Yld2k-2d yield function by incorporating an additional term to describe the yield stress and plastic flow around SH. Hu et al. (2023) developed an analytical Poly6–18p yield function by considering both SH and PST states, where two yield stresses under SH are included in the analytical determination of parameters. A new anisotropic-asymmetric yield function based on the NAFR was proposed by Hou et al. (2023b) to cover wider stress states in sheet metal forming, where both the yield stress and plastic flow under SH can be considered. In Table 1, existing isotropic and anisotropic plasticity models along with their respective features including calibration related to SH are summarized. It should be noted that recently Zhang and Lou (2024) introduced a five-parameter isotropic stress-invariant-based yield function, which includes an optional parameter determination utilizing the yield stress under SH loading. However, the current version does not account for plastic anisotropy in yield stress under SH state. Most recently, Zheng and Yoon (2024) proposed a new isotropic yield criterion under the NAFR to model the initial yield and hardening behavior across six distinct stress states including SH. They further extended this to an anisotropic model by replacing the von Mises effective stress term with a modified Hill48 yield function. While the model accurately predicts anisotropic yield and flow stress in the UT state, it struggles to capture the loading direction dependence in the SH state.

The developments and advancements outlined in Table 1 stand as noteworthy contributions to the plasticity community. However, despite these strides, several research gaps remain. Notably, none of the existing models can effectively deliver both accurate predictions of full plastic anisotropy under SH loading conditions and evade the non-physical artifacts of SH elucidated by Abedini et al. (2018). Consequently, there emerges a clear imperative to develop a plasticity model that effectively describe SHDD, offering both high precision and flexibility. The proposed stress triaxiality-dependent general framework for SHDD, namely STGF-YLD-SH, in Table 1 provides solutions to address the research void related to SHDD.

This work was divided into the following sections. The newly proposed general plasticity framework for SHDD was introduced in Section 2. The application of the new general framework to an isotropic stress-invariant-based yield function proposed by Hou et al. (2022b) and its verification are clarified in Section 3. Section 4 presents several interesting case studies of the general framework, showcasing its efficacy in modeling various materials and wide loading conditions. Besides, in Section 5, the crucial role of a governing function on the yield locus around SH was explored, shedding light on its effect on the convexity of yield surface. The calibration and validation of the proposed general plasticity framework based on the experimental data are presented in Section 6. Section 7 discusses

Table 1
Plasticity modeling of SHDD in sheet metals.

Plasticity model	Iso- or anisotropic	Flow rule	SH related calibration	SH constraint
Bassani (1977)	ISO	AFR	σ_{SH}	No
Budiansky (1984)		AFR		
Bai and Wierzbicki (2008)		AFR		
Lou et al. (2020)		NAFR		
Lou et al. (2022)		NAFR		
Zhang and Lou (2024)		NAFR		
Zheng and Yoon (2024)		NAFR		
Barlat and Lian (1989)	ANISO	AFR	σ_{SH0}, σ_{SH45}	No
Ferron et al. (1994)		AFR	σ_{SH45}	No
Vegter and Boogaard (2006)		AFR	σ_{SH0}, σ_{SH45}	No
Abedini et al. (2018)		AFR	/	Yes ($r_{SH45} = -1$)
Hao and Dong (2020)		AFR	σ_{SH0}	No
Hu et al. (2021)		AFR	σ_{SH0}, σ_{SH45}	No
Du et al. (2022)		AFR	σ_{SH0}, σ_{SH45}	No
He et al. (2022)		AFR	σ_{SH45}, r_{SH45}	No
Hu et al. (2023)		AFR	σ_{SH0}, σ_{SH45}	No
Hou et al. (2023b)		NAFR	σ_{SH45}, r_{SH45}	No
Zheng and Yoon (2024)		NAFR	σ_{SH45}	No
The present STGF-YLD-SH	ISO or ANISO	AFR or NAFR	σ_{SH0}, $\sigma_{SH22.5}$, σ_{SH45}	Yes ($r_{SH45} = -1$)

the intrinsic shear constraint, adjustable modeling of SH plastic anisotropy and simultaneous capture of shear anisotropy and tension-compression asymmetry (TCA) within the general framework. Overall, this study endeavors to provide a robust and comprehensive solution (framework) to address the SHDD in sheet metals, contributing to the advancement of plasticity modeling.

2. A general plasticity framework for shear-dominated deformation

In this work, a novel yet simple general framework for SHDD, i.e., STGF-YLD-SH, was developed as follows:

$$\Phi(\boldsymbol{\sigma}) = \omega \cdot \Phi_{SH}(\boldsymbol{\sigma}) + (1-\omega) \cdot \Phi_{TC}(\boldsymbol{\sigma}) = \sigma_Y(\bar{\varepsilon}_p), \tag{1}$$

where $\Phi(\boldsymbol{\sigma})$ represents the whole yield function in terms of the Cauchy stress tensor $\boldsymbol{\sigma}$, ω is a weighting factor or state variable, $\Phi_{SH}(\boldsymbol{\sigma})$ and $\Phi_{TC}(\boldsymbol{\sigma})$ are two distinct yield functions used to separately describe the yield behavior of materials under SHDD and tension (and compression) loading conditions. The material experiences elastic deformation when $\Phi(\boldsymbol{\sigma})$ is below the reference yield stress σ_Y, transitioning to plastic deformation when $\Phi(\boldsymbol{\sigma})$ equals σ_Y. $\bar{\varepsilon}_p$ denotes the equivalent plastic strain, namely EPS. The expressions for the yield function $\Phi_{SH}(\boldsymbol{\sigma})$ and $\Phi_{TC}(\boldsymbol{\sigma})$ are provided in a general form:

$$\Phi_\Theta(\boldsymbol{\sigma}) = \phi_\Theta(\boldsymbol{\sigma}, n_\Theta, \boldsymbol{p}_\Theta) \quad \Theta = \text{SH or TC}, \tag{2}$$

where Θ is an important subscript SH or TC to represent the SHDD or tension (compression) state. Theoretically, any isotropic or anisotropic yield function ϕ_Θ under the AFR or NAFR can be used to capture the yield behavior under the corresponding state. n_Θ and $\boldsymbol{p}_\Theta$ are the exponent constant and parameter vector, respectively. If the studied material exhibits TCA, then the yield function with TCA, such as CB2004 (Cazacu and Barlat, 2004) or CPB2006 (Cazacu et al., 2006), can be set to $\Phi_{TC}(\boldsymbol{\sigma})$. The weighting factor ω was set as a function of the stress triaxiality η with two mathematical constraints under plane stress condition initially:

$$\omega = g(\eta) = \begin{cases} 1, & \text{when } \eta = 0 \\ 0, & \text{when } |\eta| \geq 1/3 \end{cases}. \tag{3}$$

The stress triaxiality η is calculated as follows (Hu et al., 2017a):

$$\eta = \frac{\sigma_m}{\bar{\sigma}_{vM}}, \tag{4}$$

$$\sigma_{\mathrm{m}} = \frac{1}{3}(\sigma_1 + \sigma_2 + \sigma_3), \tag{5}$$

$$\overline{\sigma}_{\mathrm{vM}} = \sqrt{\frac{3}{2}\left(s_1^2 + s_2^2 + s_3^2\right)}, \tag{6}$$

$$s_i = \sigma_i - \sigma_{\mathrm{m}}, \quad i = 1, 2, 3, \tag{7}$$

where σ_{m} and $\overline{\sigma}_{\mathrm{vM}}$ are the mean stress and von Mises effective stress, respectively, σ_1, σ_2, and σ_3 are the principal stresses, s_1, s_2, and s_3 are the principal deviatoric stresses. It is noted that the local shape of yield surface predicted by Eq. (1) will be affected by the form of the employed governing function $g(\eta)$, which will be further discussed in Section 5.

Fig. 3 clarifies the schematic concept of the proposed plasticity model framework for TCA in the previous work (Hou et al., 2023a) as well as for the modeling of SHDD in this work.

Remark #1: as depicted in Fig. 3a, the symmetric yield loci of Φ_{T} (represented by the orange dashed curve) and Φ_{C} (sky-blue dashed curve) are juxtaposed in the normal plane for comparison. In the first quadrant of stress space, where $\mu = 1$, the yield locus corresponds to predictions from Φ_{T}; conversely, in the third quadrant with $\mu = 0$, the yield locus corresponds to calculations derived from Φ_{C}. This signifies that the disparity in plastic deformation exhibited by the material under tensile and compression loading conditions can be accurately described by the plasticity framework presented in Fig. 3a. An advantageous aspect of this framework is the independent characterization of plastic anisotropy in tension-dominated deformation and the calibration of model parameters in Φ_{T}, distinct from the description of compression-dominated deformation and parameter calibration in Φ_{C} (Hou et al., 2023a). These aspects can be calibrated and validated separately beforehand and subsequently integrated within the framework using the weighting factor μ. Furthermore, depending on variations in the complexity of tensile and compression loading experiments and the precision required during the sheet metal forming process, the tension-dominated yield function (Φ_{T}) can adopt relatively intricate or advanced formulations rather than Φ_{C}. Notably, the transition of the yield locus between the second and fourth quadrants is nonlinearly governed by the weighting factor μ, varying from 0 to 1. The relationship between the weighting factor μ and stress triaxiality η was meticulously established in the work by Hou et al. (2023a) to guarantee the convexity and smoothness of the yield locus or surface.

Remark #2: within the current plasticity model framework (STGF-YLD-SH) depicted in Fig. 3b, the yield stress and plastic flow of SHDD are accurately characterized. A specific yield criterion, i.e., Φ_{TC}, is either chosen or proposed to effectively capture the yield behavior including yield stress and *r*-values of sheet metals under tension and compression. Notably, the focus lies solely on delineating the plastic anisotropy in the first and third quadrants, obviating the necessity to consider its characteristics in SHDD (i.e., the second and fourth quadrants in Fig. 3b). On the contrary, the plastic anisotropy in SH is described using a specialized yield function, denoted as Φ_{SH} (illustrated by the sky-blue dashed curve). In this study, either the Hill48 or Poly4 yield function is employed, and a detailed discussion is provided in Section 7.2 (see Table 7). The comprehensive yield function is constructed as a linear combination of Φ_{TC} and Φ_{SH}, with a weighting factor ω governing this combination. The transition of the yield locus from SH

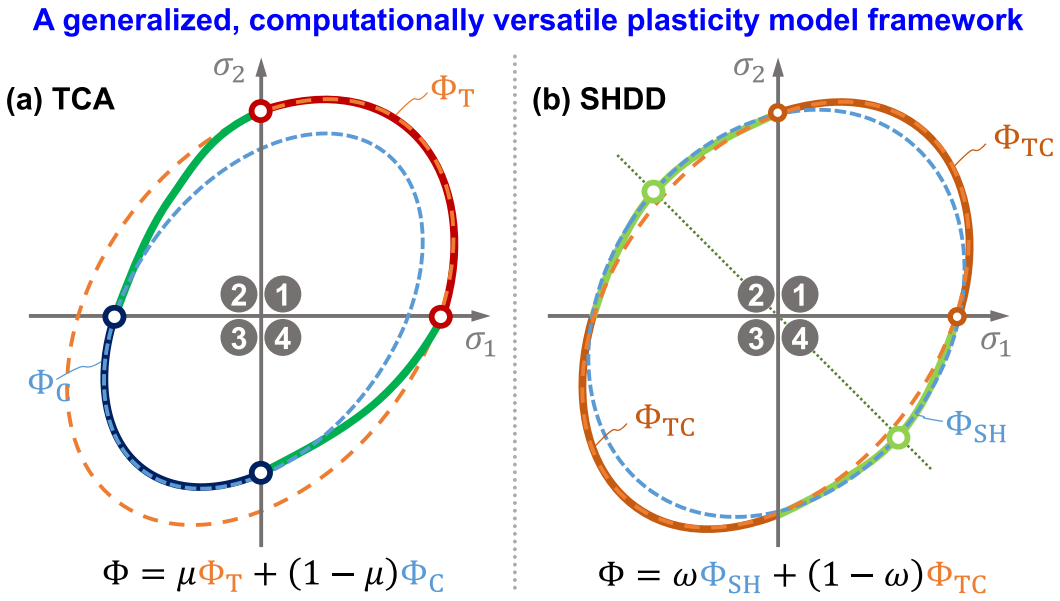

Fig. 3. Conceptual overview of the proposed generalized plasticity model framework aimed at addressing (a) TCA as discussed in Hou et al. (2023a), and (b) SHDD in this present work.

to tension or compression is regulated by the evolution of ω as a function of stress triaxiality η, as outlined in Eq. (3). The governing function $g(\eta)$, subject to mathematical constraints, influences the local shape and curvature of the yield locus around SH loading conditions. Specifically, when subjected to SH loading ($\eta = 0$), $\omega = 1$, aligning with the predictions from Φ_{SH}. Conversely, in regions dominated by tension or compression, $\omega = 0$, indicating that the yield behavior of material is described by Φ_{TC} merely. Consequently, this newly proposed plasticity model framework (STGF-YLD-SH) adeptly characterizes the plastic anisotropy of materials under both tension (or compression) and SH deformation simultaneously. Moreover, this framework is adaptable to various yield criteria, including isotropic and anisotropic criteria, as well as the AFR and NAFR plasticity models.

3. Application to the isotropic stress-invariant-based yield function (STGF-SI-Hou22-SH)

This section presents the application of the isotropic stress-invariant-based yield function within the proposed STGF-YLD-SH framework. Hou et al. (2022b) introduced an isotropic stress-invariant-based yield function, denoted as the SI-Hou22 model:

$$f_{\text{SI-Hou22}}(J_2, J_3, c) = \left(\frac{27 \cdot 3^n}{27 - 4c}\right)^{1/2n} \cdot J_2^{1/2} \cdot \left(1 - c\frac{J_3^2}{J_2^3}\right)^{1/2n} = \sigma_{\text{UT}}. \tag{8}$$

The shape-dominating parameter c was introduced to accommodate the influence of J_3 on yield behavior. The constant exponent n and the reference yield stress under UT along the RD are also defined. Remarkably, when the exponent factor n is set to 8, the modeling boundary of the yield surface reaches its maximum, demonstrating a vast variation range of yield stress under plane strain (PS) and SH conditions. Therefore, the exponent factor n of SI-Hou22 was set to 8. The SI-Hou22 model is adept at representing the convex yield surfaces of various materials. The limits of c to ensure the convexity of yield surface is $[-28.9,\ 5.47]$. The normalized yield stresses under PST and SH conditions are dependent on c, derived as follows:

$$\frac{\sigma_{\text{PS}}}{2\sigma_{\text{UT}}} = \frac{\sigma_{\text{SH}}}{\sigma_{\text{UT}}} = \left(\frac{27 - 4c}{3^{11}}\right)^{1/16}. \tag{9}$$

As elucidated by Hou et al. (2022b), the calculated yield stresses under PST and SH exhibit a broad and adjustable range based on different c. However, accurately describing the distinct initial yielding and strain hardening behaviors between SH and PST remains challenging. The predicted yield stresses under PST and SH conditions are delineated by a positive linear relationship, as expressed in Eq. (9). Henceforth, the STGF-YLD-SH framework was implemented in SI-Hou22 to delineate the distinctive yield behavior under SH and PST loadings:

$$\Phi(\boldsymbol{\sigma}) = \omega \cdot f_{\text{SI-Hou22}}(J_2, J_3, c_{\text{SH}}) + (1 - \omega) \cdot f_{\text{SI-Hou22}}(J_2, J_3, c_{\text{TC}}) = \sigma_{\text{Y}}(\bar{\varepsilon}_{\text{p}}), \tag{10}$$

where two different shape-dominating parameters c_{SH} and c_{TC} are introduced. Two illustrative instances of the 3D yield surface, as characterized by the STGF-SI-Hou22-SH yield function, are depicted in Fig. 4. These 3D yield surfaces were analytically calculated using a spherical coordinate system to account for all types of 3D stress states. In Fig. 4a, the yield surface demonstrates notably low yield stress under PST loading conditions and exceptionally high yield stress under SH loading conditions. Moreover, it is evident that the yield surface exhibits minimal local curvature in the PST state, whereas it demonstrates significant curvature in the SH state. Conversely, Fig. 4b exhibits the result diametrically opposite to those observed in Fig. 4a. The depiction in Fig. 4 elucidates that the novel STGF-SI-Hou22-SH yield function can effectively characterize the shape of a distinct yield surface, a depiction unattainable through the original SI-Hou22 yield function.

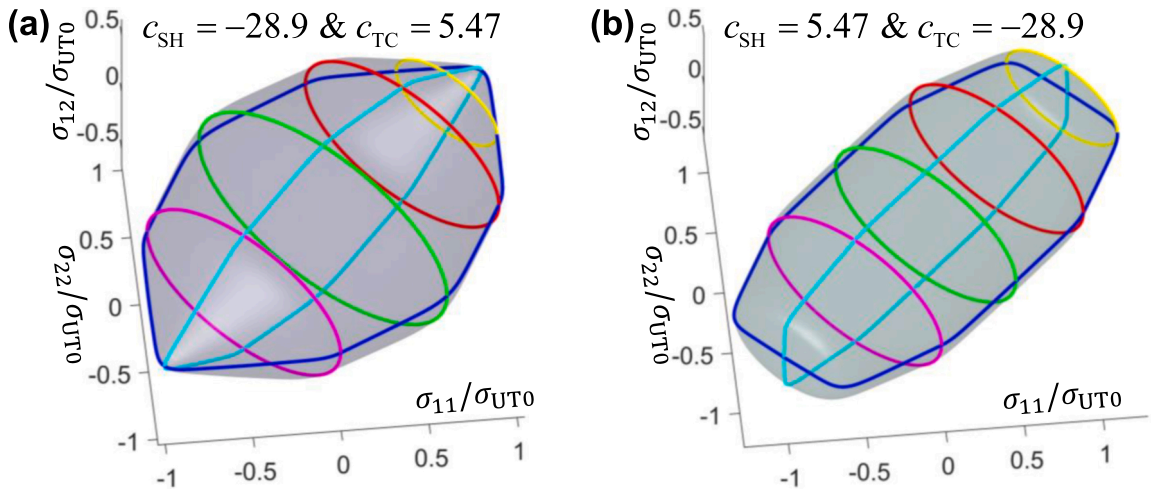

Fig. 4. Visualization of the 3D yield surface using the STGF-SI-Hou22-SH yield function showcasing materials with stress state-dependent yield stress: (a) characterized by low σ_{PS} and high σ_{SH}, and (b) featuring high σ_{PS} and low σ_{SH}.

Fig. 5 presents a two series of yield loci calculated by the STGF-SI-Hou22-SH yield function with various c_{SH}, where the other shape-dominated parameter c_{TC} is set to two limiting values: 5.47 in Fig. 5a and −28.9 in Fig. 5b. The yield loci in the normal plane, presented in Fig. 5, were analytically calculated using a polar coordinate system to generate the biaxial loadings. The predicted yield stress under SH loading (σ_{SH}) decreases with increasing c_{SH}, irrespective of c_{TC}. Thus, the STGF-SI-Hou22-SH yield function demonstrates independent descriptions of yield stress under both SH and PST loadings. To effectively illustrate the influence of two independent parameters c_{SH} and c_{TC}, the SPR value is newly defined as twice the ratio of the principal stress under SH to that under PS:

$$\mathrm{SPR} = 2\frac{\sigma_{SH}}{\sigma_{PS}}. \tag{11}$$

The SPR contour of the STGF-SI-Hou22-SH at various $c_{SH} \in [-28.9,\ 5.47]$ and $c_{TC} \in [-28.9,\ 5.47]$ is presented in Fig. 6. The STGF-SI-Hou22-SH attains an adaptive range of yield surface shapes with SPR values ranging from 0.81 to 1.23, a significantly widened range compared to the SI-Hou22 yield function, which maintains a fixed SPR value of 1. The fixed SPR value of 1 in SI-Hou22 is visually represented by the red dashed line. The magenta solid curve and blue dashed curve in Fig. 6 correspond to Fig. 5a (where $c_{TC} = 5.47$) and Fig. 5b (where $c_{TC} = -28.9$), respectively.

The experiment data of an isotropic AA7075-T6 sheet from Lou et al. (2020) was used to validate the developed STGF-SI-Hou22-SH yield function. The combined Swift-Voce hardening law was utilized to describe the strain hardening curves of AA7075-T6 under various loading conditions (Table 2). Note that 0.5 was set as the combining factor between Swift and Voce hardening laws. The two shape-dominating c_{SH} and c_{TC} evolving in terms of EPS ($\bar{\varepsilon}_p$) in the isotropic STGF-SI-Hou22-SH yield function can be analytically determined as follows:

$$c_{SH}(\bar{\varepsilon}_p) = \frac{1}{4}\left[27 - 3^{11}\left(\frac{\sigma_{SH}(\bar{\varepsilon}_p)}{\sigma_{UT}(\bar{\varepsilon}_p)}\right)^{16}\right], \tag{12}$$

and

$$c_{TC}(\bar{\varepsilon}_p) = \frac{1}{4}\left[27 - 3^{11}\left(\frac{\sigma_{PS}(\bar{\varepsilon}_p)}{2\sigma_{UT}(\bar{\varepsilon}_p)}\right)^{16}\right]. \tag{13}$$

The predicted yield loci at various EPS, i.e., 0.00, 0.03, 0.09, and 0.30, are presented in Fig. 7a. Given the unavailability of flow stress data for EBT from Lou et al. (2020), it is assumed to be equal to that under UT loading. The predicted results match very well with the experimental data in Fig. 7a. The curvature of the yield locus for the investigated AA7075-T6 decreases in the PST and SH region as EPS increases, which was accurately described by the STGF-SI-Hou22-SH. The yield stress vs. EPS curves under various stress states are depicted in Fig. 7b, and the evolution of shape-dominating parameters c_{SH} and c_{TC} in terms of EPS are presented in Fig. 7c. Interestingly, both c_{SH} and c_{TC} increase with increasing EPS. c_{TC} increases rapidly at small strains and then slowly increases to a saturated value. This is consistent with the reduced curvature of the yield locus in the PST region of AA7075-T6 in Fig. 7a.

4. Application to existing anisotropic yield functions

In this section, the application of the STGF-YLD-SH framework to various anisotropic yield functions will be investigated. The formulations of these yield functions along with the procedure for parameter identification will be detailed.

4.1. Anisotropic non-quadratic yield function (STGF-Yld2k-2d-SH)

Barlat et al. (2003) proposed the non-quadratic Yld2k-2d yield function with 8 anisotropic parameters under the AFR for plane stress condition. Here, Yld2k-2d was employed in the proposed stress triaxiality-dependent general framework for SHDD, namely STGF-Yld2k-2d-SH. The yield function $\Phi_{TC}(\boldsymbol{\sigma})$ in Eq. (1) when constructing STGF-Yld2k-2d-SH is defined as (Barlat et al., 2003):

$$\Phi_{TC}(\boldsymbol{\sigma}) = \left(\frac{\phi' + \phi''}{2}\right)^{1/m}, \tag{14}$$

$$\phi' = |X'_1 - X'_2|^m, \tag{15}$$

$$\phi'' = |2X''_2 + X''_1|^m + |2X''_1 + X''_2|^m, \tag{16}$$

where X'_k and X''_k ($k = 1,2$) are the principal values of the second-order tensors ($\boldsymbol{X}'$ and $\boldsymbol{X}''$) based on two linear transformations of the plane stress deviator. The principal values are calculated:

$$\begin{cases} X'_1 = \frac{1}{2}(X'_{11} + X'_{22}) + \frac{1}{2}\sqrt{(X'_{11} - X'_{22})^2 + 4X'^2_{12}} \\ X'_2 = \frac{1}{2}(X'_{11} + X'_{22}) - \frac{1}{2}\sqrt{(X'_{11} - X'_{22})^2 + 4X'^2_{12}} \end{cases}, \tag{17}$$

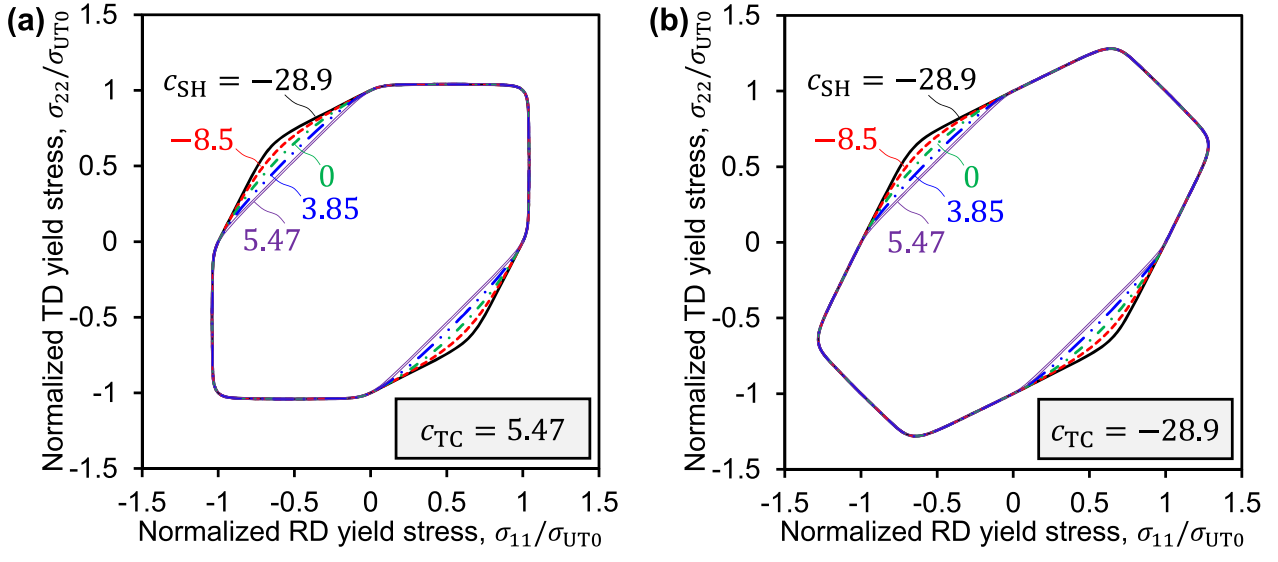

Fig. 5. Yield loci in the normal plane predicted by the STGF-SI-Hou22-SH yield function illustrating variations with different values of c_{TC}: (a) $c_{TC} = 5.47$ and (b) $c_{TC} = -28.9$.

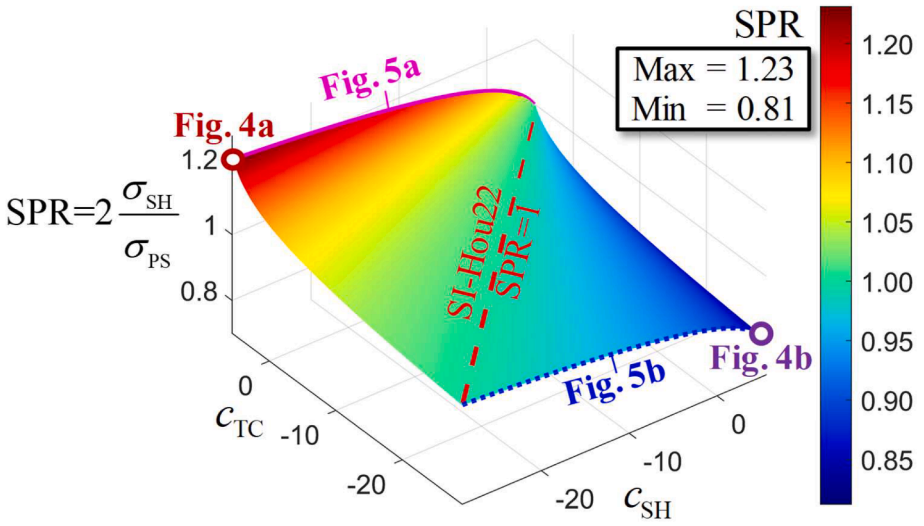

Fig. 6. Effect of parameters c_{TC} and c_{SH} on the SPR value ($=2\sigma_{SH}/\sigma_{PS}$) calculated by the STGF-SI-Hou22-SH yield function.

Table 2
Parameters of AA7075-T6 in the combined Swift-Voce hardening law under various states.

Combined Swift-Voce law	$\sigma(\bar{\varepsilon}_p) = \frac{1}{2}\{K_{SV}(\bar{\varepsilon}_p+\varepsilon_0)^{n_{SV}} + [A_{SV} - (A_{SV}-B_{SV})\cdot\exp(-C_{SV}\bar{\varepsilon}_p)]\}$					
Parameter	K_{SV} (MPa)	ε_0	n_{SV}	A_{SV} (MPa)	B_{SV} (MPa)	C_{SV}
UT	871.15	0.0422	0.1630	748.44	536.35	10.592
PS	792.30	0.0414	0.1680	679.77	565.36	10.455
SH	761.40	0.0479	0.1574	731.44	555.83	12.662

$$\begin{cases} X''_1 = \frac{1}{2}(X''_{11}+X''_{22}) + \frac{1}{2}\sqrt{(X''_{11}-X''_{22})^2+4X''^2_{12}} \\ X''_2 = \frac{1}{2}(X''_{11}+X''_{22}) - \frac{1}{2}\sqrt{(X''_{11}-X''_{22})^2+4X''^2_{12}} \end{cases}. \tag{18}$$

The two tensors $\boldsymbol{X}'$ and $\boldsymbol{X}''$ are obtained from:

$$\begin{bmatrix} X'_{11} \\ X'_{22} \\ X'_{12} \end{bmatrix} = \boldsymbol{L}' \begin{bmatrix} \sigma_{11} \\ \sigma_{22} \\ \sigma_{12} \end{bmatrix} = \begin{bmatrix} L'_{11} & L'_{12} & 0 \\ L'_{21} & L'_{22} & 0 \\ 0 & 0 & L'_{66} \end{bmatrix} \begin{bmatrix} \sigma_{11} \\ \sigma_{22} \\ \sigma_{12} \end{bmatrix}, \tag{19}$$

$$\begin{bmatrix} X''_{11} \\ X''_{22} \\ X''_{12} \end{bmatrix} = \boldsymbol{L}'' \begin{bmatrix} \sigma_{11} \\ \sigma_{22} \\ \sigma_{12} \end{bmatrix} = \begin{bmatrix} L''_{11} & L''_{12} & 0 \\ L''_{21} & L''_{22} & 0 \\ 0 & 0 & L''_{66} \end{bmatrix} \begin{bmatrix} \sigma_{11} \\ \sigma_{22} \\ \sigma_{12} \end{bmatrix}, \tag{20}$$

where σ_{11} and σ_{22} are the stress components along the RD and transverse direction (TD), respectively, and σ_{12} is the in-plane shear stress component. The components of the linear transformation tensors, $\boldsymbol{L}'$ and $\boldsymbol{L}''$, are expressed with a set of Yld2k-2d parameters ($\alpha_1 \sim \alpha_8$):

$$\begin{bmatrix} L'_{11} \\ L'_{12} \\ L'_{21} \\ L'_{22} \\ L'_{66} \end{bmatrix} = \frac{1}{3}\begin{bmatrix} 2 & 0 & 0 \\ -1 & 0 & 0 \\ 0 & -1 & 0 \\ 0 & 2 & 0 \\ 0 & 0 & 3 \end{bmatrix} \begin{bmatrix} \alpha_1 \\ \alpha_2 \\ \alpha_7 \end{bmatrix}, \tag{21}$$

$$\begin{bmatrix} L''_{11} \\ L''_{12} \\ L''_{21} \\ L''_{22} \\ L''_{66} \end{bmatrix} = \frac{1}{9}\begin{bmatrix} -2 & 2 & 8 & -2 & 0 \\ 1 & -4 & -4 & 4 & 0 \\ 4 & -4 & -4 & 1 & 0 \\ -2 & 8 & 2 & -2 & 0 \\ 0 & 0 & 0 & 0 & 9 \end{bmatrix} \begin{bmatrix} \alpha_3 \\ \alpha_4 \\ \alpha_5 \\ \alpha_6 \\ \alpha_8 \end{bmatrix}. \tag{22}$$

The Yld2k-2d function can capture the yield stresses and *r*-values under UT along the RD, 45° to the RD (diagonal direction, DD),

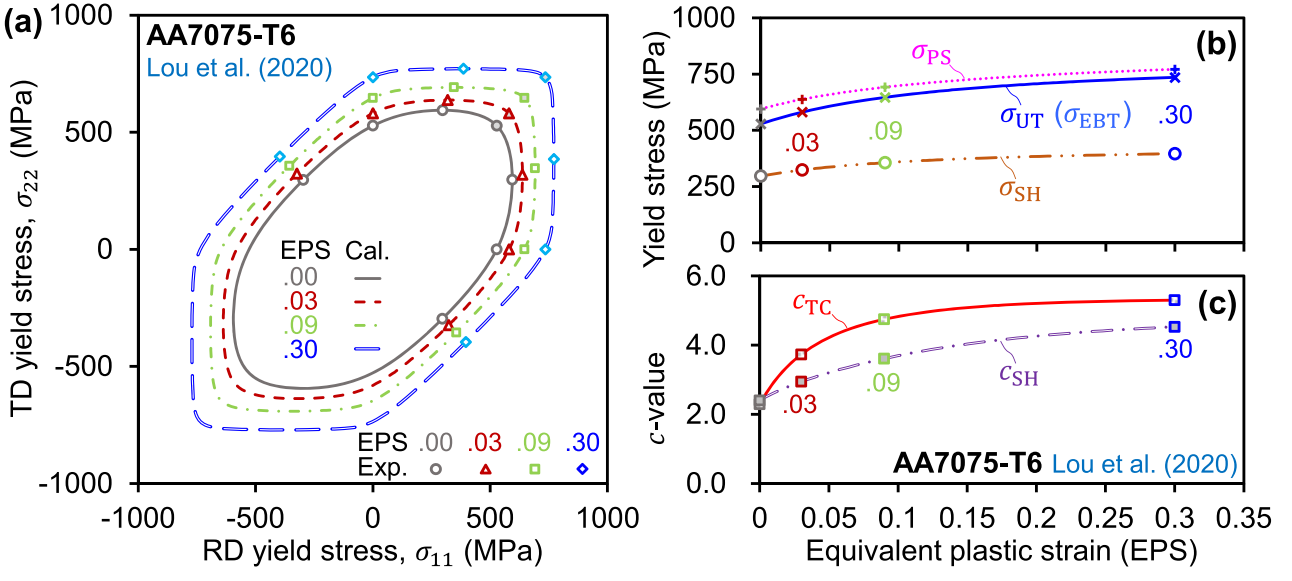

Fig. 7. (a) Predicted yield loci of AA7075-T6 at various EPS levels using the STGF-SI-Hou22-SH yield function; (b) predicted stress-strain curves of AA7075-T6 under various stress states; (c) evolution of shape-dominating parameters c_{SH} and c_{TC} as functions of EPS.

and TD as well as EBT simultaneously. The exponent m can be determined based on the crystal structure or the measured yield stresses under PST loading. The 8 parameters require calibration with the experimental data as presented in Eq. (23) to minimize the error function in Eq. (24).

$$[\sigma_{\mathrm{UT0}} \quad \sigma_{\mathrm{UT45}} \quad \sigma_{\mathrm{UT90}} \quad \sigma_{\mathrm{EBT}} \quad r_{\mathrm{UT0}} \quad r_{\mathrm{UT45}} \quad r_{\mathrm{UT90}} \quad r_{\mathrm{EBT}}] \triangleright\triangleright [\alpha_1 \sim \alpha_8], \tag{23}$$

$$\mathrm{Err} = \sum_{i=0}^{2} \left(\left| \frac{\sigma^{\mathrm{cal.}}_{\mathrm{UTi{\cdot}45}}}{\sigma^{\mathrm{exp.}}_{\mathrm{UTi{\cdot}45}}} - 1 \right| + \left| \frac{r^{\mathrm{cal.}}_{\mathrm{UTi{\cdot}45}}}{r^{\mathrm{exp.}}_{\mathrm{UTi{\cdot}45}}} - 1 \right| \right) + \left| \frac{\sigma^{\mathrm{cal.}}_{\mathrm{EBT}}}{\sigma^{\mathrm{exp.}}_{\mathrm{EBT}}} - 1 \right| + \left| \frac{r^{\mathrm{cal.}}_{\mathrm{EBT}}}{r^{\mathrm{exp.}}_{\mathrm{EBT}}} - 1 \right|, \tag{24}$$

where 'cal.' and 'exp.' in the superscripts indicate the calculated and experimental results, respectively.

The yield function $\Phi_{\mathrm{SH}}(\boldsymbol{\sigma})$ in Eq. (1) to capture SH loading is newly proposed as a simple quadratic function:

$$\Phi_{\mathrm{SH}}(\boldsymbol{\sigma}) = \sqrt{\sigma_{11}^2 + \sigma_{22}^2 - n_1\sigma_{11}\sigma_{22} + 3n_2\sigma_{12}^2}, \tag{25}$$

where n_1 and n_2 are two parameters related to SH, which can be directly identified from yield stresses under SH along two loading directions, namely σ_{SH45} and σ_{SH0}:

$$n_1 = \left(\frac{\sigma_{\mathrm{UT0}}}{\sigma_{\mathrm{SH45}}}\right)^2 - 2, \quad n_2 = \frac{1}{3}\left(\frac{\sigma_{\mathrm{UT0}}}{\sigma_{\mathrm{SH0}}}\right)^2. \tag{26}$$

4.2. Anisotropic polynomial yield function (STGF-Poly6-SH)

The proposed framework can also adopt complex yield functions $\Phi_{\mathrm{TC}}(\boldsymbol{\sigma})$ to improve the prediction accuracy. A sixth-order polynomial yield function, Poly6, is used as $\Phi_{\mathrm{TC}}(\boldsymbol{\sigma})$ to model yield stresses and r-values under a wide range of stress states (Du et al., 2022):

$$\Phi_{\mathrm{TC}}(\boldsymbol{\sigma}) = \begin{pmatrix} a_1\sigma_{11}^6 + a_2\sigma_{11}^5\sigma_{22} + a_3\sigma_{11}^4\sigma_{22}^2 + a_4\sigma_{11}^3\sigma_{22}^3 + a_5\sigma_{11}^2\sigma_{22}^4 + a_6\sigma_{11}\sigma_{22}^5 + a_7\sigma_{22}^6 \\ +\left(a_8\sigma_{11}^4 + a_9\sigma_{11}^3\sigma_{22} + a_{10}\sigma_{11}^2\sigma_{22}^2 + a_{11}\sigma_{11}\sigma_{22}^3 + a_{12}\sigma_{22}^4\right)\sigma_{12}^2 \\ +\left(a_{13}\sigma_{11}^2 + a_{14}\sigma_{11}\sigma_{22} + a_{15}\sigma_{22}^2\right)\sigma_{12}^4 \\ +a_{16}\sigma_{12}^6 \end{pmatrix}^{1/6}, \tag{27}$$

where a_i ($i = 1 \sim 16$) are model parameters. By combining the Poly6 function in Eq. (27) and the quadratic function in Eq. (25) within the proposed framework, namely STGF-Poly6-SH, a comprehensive and accurate representation of the anisotropic yield stresses and r-values of sheet metals under both tension and shear were achieved.

Regarding the parameter identification of Poly6 function, a new analytic calibration program was introduced in this work for the Poly6 yield function.

(1) Firstly, the parameters related to yield locus in the normal plane, i.e., $a_1 \sim a_7$, are calculated based on the experimental data of σ_{UT0}, r_{UT0}, σ_{UT90}, r_{UT90}, σ_{EBT}, r_{EBT}, and σ_{PST0} (or σ_{PST90}):

$$a_1 = 1, \tag{28a}$$

$$a_2 = \frac{-6r_{\mathrm{UT0}}}{r_{\mathrm{UT0}} + 1}, \tag{28b}$$

$$a_7 = \left(\frac{\sigma_{\mathrm{UT0}}}{\sigma_{\mathrm{UT90}}}\right)^6, \tag{28c}$$

$$a_6 = -\frac{6r_{\mathrm{UT90}}}{r_{\mathrm{UT90}} + 1}a_7, \tag{28d}$$

and regarding σ_{EBT} and r_{EBT}, we have

$$\left(\frac{\sigma_{\mathrm{UT0}}}{\sigma_{\mathrm{EBT}}}\right)^6 = a_1 + a_2 + a_3 + a_4 + a_5 + a_6 + a_7, \tag{29a}$$

$$r_{\mathrm{EBT}} = \frac{a_2 + 2a_3 + 3a_4 + 4a_5 + 5a_6 + 6a_7}{6a_1 + 5a_2 + 4a_3 + 3a_4 + 2a_5 + a_6}. \tag{29b}$$

Under the PST loading (σ_1:$\sigma_2 = 2$) along the RD and TD, the yield stresses, i.e., σ_{PST0} and σ_{PST90}, can be calculated. Based on the Poly6 yield function in Eq. (27), we have

$$64\left(\frac{\sigma_{\mathrm{UT0}}}{\sigma_{\mathrm{PST0}}}\right)^6 = 64a_1 + 32a_2 + 16a_{3\mathrm{R}} + 8a_4 + 4a_{5\mathrm{R}} + 2a_6 + a_7, \tag{30a}$$

$$64\left(\frac{\sigma_{\mathrm{UT0}}}{\sigma_{\mathrm{PST90}}}\right)^6 = a_1 + 2a_2 + 4a_{3\mathrm{T}} + 8a_4 + 16a_{5\mathrm{T}} + 32a_6 + 64a_7. \tag{30b}$$

By combining Eqs. (28)–(30), the anisotropic parameter, a_3 and a_5, can be solved:

(I) based on the yield stress under PST along the RD, i.e., σ_{PST0}:

$$\begin{cases} a_{3\mathrm{R}} = 16\left(\frac{\sigma_{\mathrm{UT0}}}{\sigma_{\mathrm{PST0}}}\right)^6 + \left(\frac{r_{\mathrm{EBT}}-5}{r_{\mathrm{EBT}}+1}\right)\left(\frac{\sigma_{\mathrm{UT0}}}{\sigma_{\mathrm{EBT}}}\right)^6 - 11a_1 - 4a_2 - \frac{1}{2}a_6 - \frac{5}{4}a_7 \\ a_{5\mathrm{R}} = 16\left(\frac{\sigma_{\mathrm{UT0}}}{\sigma_{\mathrm{PST0}}}\right)^6 + \left(\frac{4r_{\mathrm{EBT}}-8}{r_{\mathrm{EBT}}+1}\right)\left(\frac{\sigma_{\mathrm{UT0}}}{\sigma_{\mathrm{EBT}}}\right)^6 - 8a_1 - 2a_2 - \frac{5}{2}a_6 - \frac{17}{4}a_7 \end{cases}, \tag{31a}$$

(II) or based on the yield stress under PST along the TD, i.e., σ_{PST90}:

$$\begin{cases} a_{3\mathrm{T}} = 16\left(\frac{\sigma_{\mathrm{UT0}}}{\sigma_{\mathrm{PST90}}}\right)^6 + \left(\frac{4-8r_{\mathrm{EBT}}}{r_{\mathrm{EBT}}+1}\right)\left(\frac{\sigma_{\mathrm{UT0}}}{\sigma_{\mathrm{EBT}}}\right)^6 - \frac{17}{4}a_1 - \frac{5}{2}a_2 - 2a_6 - 8a_7 \\ a_{5\mathrm{T}} = 16\left(\frac{\sigma_{\mathrm{UT0}}}{\sigma_{\mathrm{PST90}}}\right)^6 + \left(\frac{1-5r_{\mathrm{EBT}}}{r_{\mathrm{EBT}}+1}\right)\left(\frac{\sigma_{\mathrm{UT0}}}{\sigma_{\mathrm{EBT}}}\right)^6 - \frac{5}{4}a_1 - \frac{1}{2}a_2 - 4a_6 - 11a_7 \end{cases}. \tag{31b}$$

In this work, in order to give an accurate and balanced prediction of the yield stress under PST along different loading directions, an average value is calculated as the identified parameter as follows:

$$\begin{cases} a_3 = \frac{1}{2}(a_{3\mathrm{R}} + a_{3\mathrm{T}}) \\ a_5 = \frac{1}{2}(a_{5\mathrm{R}} + a_{5\mathrm{T}}) \end{cases}, \tag{32}$$

i.e.,

$$\begin{cases} a_3 = 8\left(\frac{\sigma_{\mathrm{UT0}}}{\sigma_{\mathrm{PST0}}}\right)^6 + 8\left(\frac{\sigma_{\mathrm{UT0}}}{\sigma_{\mathrm{PST90}}}\right)^6 - \frac{1}{2}\left(\frac{1+7r_{\mathrm{EBT}}}{r_{\mathrm{EBT}}+1}\right)\left(\frac{\sigma_{\mathrm{UT0}}}{\sigma_{\mathrm{EBT}}}\right)^6 - \frac{61}{8}a_1 - \frac{13}{4}a_2 - \frac{5}{4}a_6 - \frac{37}{8}a_7 \\ a_5 = 8\left(\frac{\sigma_{\mathrm{UT0}}}{\sigma_{\mathrm{PST0}}}\right)^6 + 8\left(\frac{\sigma_{\mathrm{UT0}}}{\sigma_{\mathrm{PST90}}}\right)^6 - \frac{1}{2}\left(\frac{7+r_{\mathrm{EBT}}}{r_{\mathrm{EBT}}+1}\right)\left(\frac{\sigma_{\mathrm{UT0}}}{\sigma_{\mathrm{EBT}}}\right)^6 - \frac{37}{8}a_1 - \frac{5}{4}a_2 - \frac{13}{4}a_6 - \frac{61}{8}a_7 \end{cases}. \tag{33}$$

Then the parameter a_4 is calibrated as shown in Eq. (34):

$$a_4 = \left(\frac{\sigma_{\mathrm{UT0}}}{\sigma_{\mathrm{EBT}}}\right)^6 - (a_1 + a_2 + a_3 + a_5 + a_6 + a_7). \tag{34}$$

(2) Secondly, there is an independent parameter a_{16}, which is related to the vertex of the yield surface. Hu et al. (2021) suggested that the σ_{SH0} value corresponding to the SH condition along the RD can be used to determine a_{16} as a straightforward means:

$$a_{16} = \left(\frac{\sigma_{\mathrm{UT0}}}{\sigma_{\mathrm{SH0}}}\right)^6. \tag{35}$$

However, the shear anisotropy can be accurately captured by the quadratic σ_{SH} function (Eq. (25)) within the proposed plasticity framework. Additionally, Eq. (26) provide direct parameter calibration for shear anisotropy. Consequently, a novel identification method without SH data was introduced here to determine a_{16}, enhancing the accuracy in describing yield stress anisotropy of sheet metal under PST loading. A preset a_{16} value from 20 to 40 is assigned, based on which the remaining eight parameters ($a_8 \sim a_{15}$) can be determined from the UT data. Hou et al. (2020) reported that advanced high-strength steels and Al alloys usually exhibit a strong orientation dependence in the Lankford coefficient rather than yield stress. Hence, five *r*-values and three UT yield stresses are used in this work for the identification of $a_8 \sim a_{15}$. Please refer to Hou et al. (2023a) for details. After that, the yield stress under PST loading along the DD, i.e., σ_{PST45}, can be directly calculated as follows:

$$\sigma_{\mathrm{PST45}} = \frac{4\sigma_{\mathrm{UT0}}}{\left[\begin{array}{l}(a_1+a_2+a_3+a_4+a_5+a_6+a_7)3^6 + (a_8+a_9+a_{10}+a_{11}+a_{12})3^4 \\ +(a_{13}+a_{14}+a_{15})3^2 + a_{16}\end{array}\right]^{1/6}}. \tag{36}$$

Finally, a simple traversal loop with an interval of 0.1 is employed to identify the value of a_{16} that satisfies the requirements of the Poly6 yield surface convexity and minimizes the prediction error of σ_{PST45}, thereby achieving the calibration of all 16 anisotropic parameters.

By combining Eqs. (25) and (27) within the STGF-Poly6-SH framework, an accurate representation of plastic anisotropy covering a wide range of stress states was achieved. For comparison, Table 3 summarizes several recent studies on the Poly6 yield function in the past three years. Only the newly proposed STGF-Poly6-SH can consider yield stress or plastic flow direction for all listed loading conditions, especially the yield stress under PST along the DD and the direction of plastic strain rate under EBT loading. Note that all

the Poly6 yield functions in Table 3 have the same calibration strategy regarding the UT data to identify these 12 parameters: a_1, a_2, a_6, a_7, and a_8~a_{15}. Compared with Poly6–18p proposed by Hu et al. (2023), the novel framework STGF-Poly6-SH with 18 parameters shows higher accuracy in describing the anisotropy of yield stress under PST loading. It will be verified by experimental data in Section 6. Moreover, the proposed framework offers adjustable flexibility for shear anisotropy across varying degrees of yield stress in metal sheets, which will be further discussed in Section 7.2.

The STGF-Poly6-SH framework offers a distinct advantage over the STGF-Yld2k-2d-SH by providing an analytical method for identifying anisotropic parameters. This advantage enhances its suitability for sheet metals with prominent anisotropic hardening behavior under proportional loadings.

4.3. Non-associated anisotropic non-quadratic yield function (STGF-NAFR-Min16-SH)

The newly proposed framework STGF-YLD-SH can also be applied to the NAFR. Min et al. (2016) developed a non-quadratic yield function under the NAFR considering anisotropic hardening for sheet metals, namely Min2016, where the shear anisotropy of sheet metals cannot be considered. In this sub-section, as an example of the NAFR, Min2016 was used in the proposed framework (STGF-NAFR-Min16-SH) to describe the anisotropic plastic deformation regarding the flow stresses and evaluation of r-values covering stress state of SH. The yield stress function is expressed as follows (Min et al., 2016):

$$\Phi_{\mathrm{TC}}(\boldsymbol{\sigma}) = \left[a_{\mathrm{y}}(U_1+U_2)^n + a_{\mathrm{y}}(U_1-U_2)^n + b_{\mathrm{y}}(2U_2)^n\right]^{1/n}, \tag{37}$$

with

$$U_1 = \frac{\sigma_{11}+c_{\mathrm{y}}\sigma_{22}}{2}, \tag{38a}$$

$$U_2 = \sqrt{\left(\frac{\sigma_{11}-c_{\mathrm{y}}\sigma_{22}}{2}\right)^2 + \left(d_{\mathrm{y}}\sigma_{12}\right)^2}, \tag{38b}$$

where the four parameters (a_{y}, b_{y}, c_{y}, and d_{y}) can be identified from four yield stresses, i.e., σ_{UT0}, σ_{UT45}, σ_{UT90}, and σ_{EBT}, based on Eq. (39):

$$a_{\mathrm{y}} + b_{\mathrm{y}} = 1, \tag{39a}$$

$$c_{\mathrm{y}} = \frac{\sigma_{\mathrm{UT0}}}{\sigma_{\mathrm{UT90}}}, \tag{39b}$$

$$a_{\mathrm{y}} = \frac{\left(\sigma_{\mathrm{UT0}}/\sigma_{\mathrm{EBT}}\right)^n - \left(1-c_{\mathrm{y}}\right)^n}{1+c_{\mathrm{y}}^n - \left(1-c_{\mathrm{y}}\right)^n}, \tag{39c}$$

$$a_{\mathrm{y}}\left(\frac{1+c_{\mathrm{y}}}{2}+\chi\right)^n + a_{\mathrm{y}}\left(\frac{1+c_{\mathrm{y}}}{2}-\chi\right)^n + (1-a_{\mathrm{y}})(2\chi)^n = \left(\frac{\sigma_{\mathrm{UT0}}}{\sigma_{\mathrm{UT45}}}\right)^n, \tag{39d}$$

with

$$\chi = \sqrt{\left(\frac{1-c_{\mathrm{y}}}{2}\right)^2 + d_{\mathrm{y}}^2}. \tag{40}$$

The plastic potential function in Min2016 is expressed as (Min et al., 2016):

$$\Psi_{\mathrm{TC}}(\boldsymbol{\sigma}) = \left[a_{\mathrm{p}}(V_1+V_2)^m + a_{\mathrm{p}}(V_1-V_2)^m + b_{\mathrm{p}}(2V_2)^m\right]^{1/m}, \tag{41}$$

with

Table 3
Representation of plastic anisotropy considering stress states in the Poly6 yield functions.

Plasticity model	SH		PST			EBT		UT (5σ+7r) or (7σ+5r)	
	σ_{SH0}	σ_{SH45}	σ_{PST0}	σ_{PST45}	σ_{PST90}	σ_{EBT}	r_{EBT}	σ_{UT0}~σ_{UT90}	r_{UT0}~r_{UT90}
The present STGF-Poly6-SH framework	★	★	★	★	★	★	★	★	★
Hu et al. (2023) Poly6–18p	★	★	★	☆	★	★	★	★	★
Du et al. (2022)	★	☆	★	★	★	★	☆	★	★
Hu et al. (2021) Poly6-I	★	★	☆	☆	☆	★	★	★	★
Hu et al. (2021) Poly6-II	★	☆	★	☆	★	★	☆	★	★

$$V_1 = \frac{\sigma_{11} + h_p \sigma_{22}}{2}, \tag{42a}$$

$$V_2 = \sqrt{\left(\frac{\sigma_{11} - c_p \sigma_{22}}{2}\right)^2 + \left(d_p \sigma_{12}\right)^2}, \tag{42b}$$

where the five parameters (a_p, b_p, c_p, d_p, and h_p) can be determined using Eq. (43) based on the four r-values: r_{UT0}, r_{UT45}, r_{UT90}, and r_{EBT}:

$$a_p + b_p = 1, \tag{43a}$$

$$\frac{2}{a_p(1+h_p) + 4(a_p + 2b_p)(1 - c_p)} = 1 + r_{UT0}, \tag{43b}$$

$$\frac{a_p(\kappa_1 + \kappa_2)^m + a_p(\kappa_1 - \kappa_2)^m + b_p(2\kappa_2)^m}{\left\{\begin{array}{l} \frac{1+h_p}{2}\left[a_p(\kappa_1 + \kappa_2)^{m-1} + a_p(\kappa_1 - \kappa_2)^{m-1}\right] \\ + \frac{(1-c_p)^2}{2\kappa_2}\left[a_p(\kappa_1 + \kappa_2)^{m-1} - a_p(\kappa_1 - \kappa_2)^{m-1} + 2b_p(2\kappa_2)^{m-1}\right] \end{array}\right\}} = 1 + r_{UT45}, \tag{43c}$$

$$\frac{a_p\left(\frac{h_p + c_p}{2}\right)^m + a_p\left(\frac{h_p - c_p}{2}\right)^m + b_p c_p^m}{\frac{1+h_p}{2}(\kappa_3 + \kappa_4) + 2(c_p - 1)\left(\kappa_3 - \kappa_4 + 2b_p c_p^{m-1}\right)} = 1 + r_{UT90}, \tag{43d}$$

$$r_{EBT} = \frac{\left\{\begin{array}{l} \frac{h_p}{2}\left[a_p\left(\frac{2 + h_p - c_p}{2}\right)^{m-1} + a_p\left(\frac{h_p + c_p}{2}\right)^{m-1}\right] \\ -2c_p\left[a_p\left(\frac{2 + h_p - c_p}{2}\right)^{m-1} - a_p\left(\frac{h_p + c_p}{2}\right)^{m-1} + 2b_p(1 - c_p)^{m-1}\right] \end{array}\right\}}{\left\{\begin{array}{l} \frac{1}{2}\left[a_p\left(\frac{2 + h_p - c_p}{2}\right)^{m-1} + a_p\left(\frac{h_p + c_p}{2}\right)^{m-1}\right] \\ +2\left[a_p\left(\frac{2 + h_p - c_p}{2}\right)^{m-1} - a_p\left(\frac{h_p + c_p}{2}\right)^{m-1} + 2b_p(1 - c_p)^{m-1}\right] \end{array}\right\}}, \tag{43e}$$

with

$$\kappa_1 = \frac{1 + h_p}{4}, \tag{44a}$$

$$\kappa_2 = \sqrt{\left(\frac{1 - c_p}{4}\right)^2 + \frac{1}{4}d_p^2}, \tag{44b}$$

$$\kappa_3 = a_p\left(\frac{h_p + c_p}{2}\right)^{m-1}, \tag{44c}$$

$$\kappa_4 = a_p\left(\frac{h_p - c_p}{2}\right)^{m-1}. \tag{44d}$$

Considering the capture of shear anisotropy in yield stress of sheet metals, the yield stress function in Eq. (25) as $\Phi_{SH}(\boldsymbol{\sigma})$ is coupled with the Min2016 yield stress function (Eq. (37)) within the proposed STGF-NAFR-Min16-SH. While, a simple isotropic quadrant function, i.e., Eq. (25) with two parameters of unity ($n_1 = n_2 = 1$), is combined with the Min2016 plastic potential function (Eq. (41)) within STGF-NAFR-Min16-SH to ensure the shear constraint reported in Abedini et al. (2018). The non-quadratic STGF-NAFR-Min16 model has 11 to-be-calibrated parameters in total when considering the shear anisotropy in yield stress, which requires a simpler analytic procedure for parameter determination compared to the non-quadratic yield criteria under the AFR (e.g. STGF-Yld2k-2d-SH with 10 parameters).

Regarding the numerical implementation of these plasticity models within the proposed framework into FE analyses, various algorithms such as return mapping methods have been developed (Lee et al., 2023, 2012, 2005; Liu et al., 2023b; Scherzinger, 2017). To enhance computational efficiency, Choi and Yoon (2019) proposed the Euler backward method based on finite difference method (FDM) to compute the first and second derivatives of the complex yield stress and plastic potential functions. Recently, Hu et al. (2024)

developed a simple, efficient, and user-friendly step size in FDM to calculate the derivatives of constitutive models, which has been successfully applied in FE analysis. Readers can refer to these algorithms for the relevant implementation of complex yield functions, such as STGF-NAFR-Min16-SH, to simulate the complicated sheet metal forming process.

5. Effect of weighting factor on the yield locus: convexity of the plasticity framework

In the proposed general framework, the weighting factor ω is a function of stress triaxiality η, reflecting the stress state-dependent plastic anisotropy. Here a symmetric piecewise fifth-order (SPPoly5) function is newly proposed to describe the continuous variation of ω:

$$\omega = g(\eta) = \begin{cases} 0, & \frac{1}{3} \le |\eta| \le \frac{2}{3} \\ \lambda_0 + \lambda_1|\eta| + \lambda_2|\eta|^2 + \lambda_3|\eta|^3 + \lambda_4|\eta|^4 + \lambda_5|\eta|^5, & 0 \le |\eta| < \frac{1}{3} \end{cases}. \tag{45}$$

These six constants $\lambda_0 \sim \lambda_5$ in Eq. (45) were calibrated from six mathematical constraints in Eqs. (46) and (47), which is illustrated in Fig. 8 by the hollow points. The predicted variation of ω as well as the absolute value of its first derivative in terms of η, i.e., $\partial\omega/\partial\eta$, by the SPPoly5 function within $\eta \in [-2/3, 2/3]$ is plotted in Fig. 8.

$$\begin{cases} \omega(\eta = 0) = g(0) = 1, & \text{SH loading} \\ \omega(\eta = 1/6) = g(1/6) = 0.6 & \\ \omega(\eta = 1/3) = g(1/3) = 0, & \text{UT loading} \end{cases}, \tag{46}$$

and

$$\begin{cases} \frac{\partial\omega}{\partial\eta}(\eta = 0) = 0, & \text{SH loading} \\ \frac{\partial\omega}{\partial\eta}(\eta = 1/6) = \Lambda & \\ \frac{\partial\omega}{\partial\eta}(\eta = 1/3) = 0, & \text{UT loading} \end{cases}, \tag{47}$$

where Λ represents the slope of ω vs. η curve (blue solid curve in Fig. 8) when $\eta = 1/6$, corresponding to the red hollow point *No 5* ($|\Lambda| = 3$ for example). Note that, for simplicity, a value of 0.5 or 0.6 was assigned to ω when $\eta = 1/6$, indicated by the blue hollow point *No 2* in Fig. 8. Substituting Eqs. (46) and (47) into Eq. (45), lengthy but straightforward calculations yield:

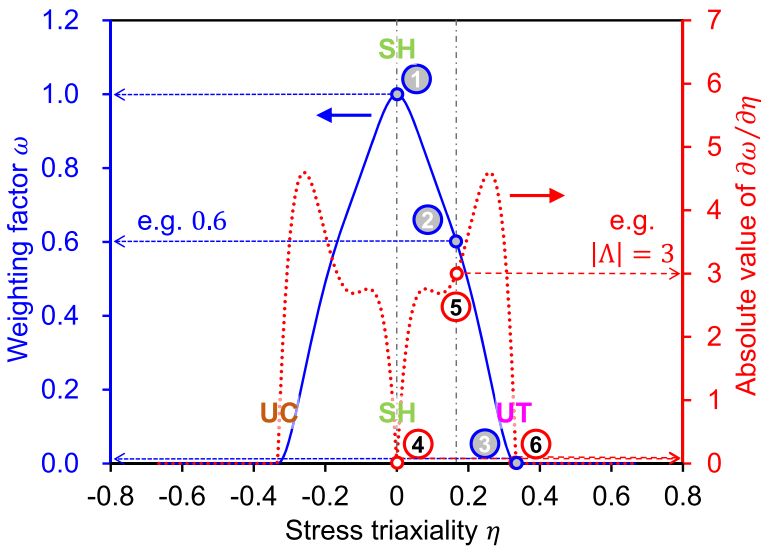

Fig. 8. Variation of weighting factor ω and its derivative $\partial\omega/\partial\eta$ as functions of stress triaxiality η in the SPPoly5 governing function constrained by six mathematical conditions.

$$\begin{bmatrix}\lambda_0\\ \lambda_1\\ \lambda_2\\ \lambda_3\\ \lambda_4\\ \lambda_5\end{bmatrix} = \begin{bmatrix}0\\ 0\\ -24\\ 288\\ -1080\\ 1296\end{bmatrix}\Lambda + \begin{bmatrix}1\\ 0\\ -120.6\\ 1263.6\\ -4730.4\\ 5832\end{bmatrix}. \tag{48}$$

To investigate the effect of the weighting factor ω on the predicted yield locus and its convexity, three different values of Λ were assigned to the SPPoly5 function to describe the evolution of ω with respect to the variation of η, as shown in Fig. 9a. As a result, the yield loci obtained using the proposed plasticity framework, which combines the Hosford72 yield function with an order of 8 as $\Phi_{TC}(\sigma)$ and the von Mises yield function as $\Phi_{SH}(\sigma)$, with three different evolutions of weighting factor ω (see Fig. 9a), are compared in Fig. 9b. The three yield loci are coincident in the first and third quadrants (Hosford72 yielding) and also coincide with the same yield point under SH loading (von Mises yielding), i.e., when the biaxial loading angle φ_L is 135° or -45°. The influence of ω is only reflected in the yield locus with φ_L ranging from 90° to 135° (considering the symmetry) in Fig. 9b. The local slope ξ of yield loci with φ_L between 90° and 135° was calculated and compared in Fig. 9c to further investigate the effect of ω on the yield locus shape. Among them, only the ξ

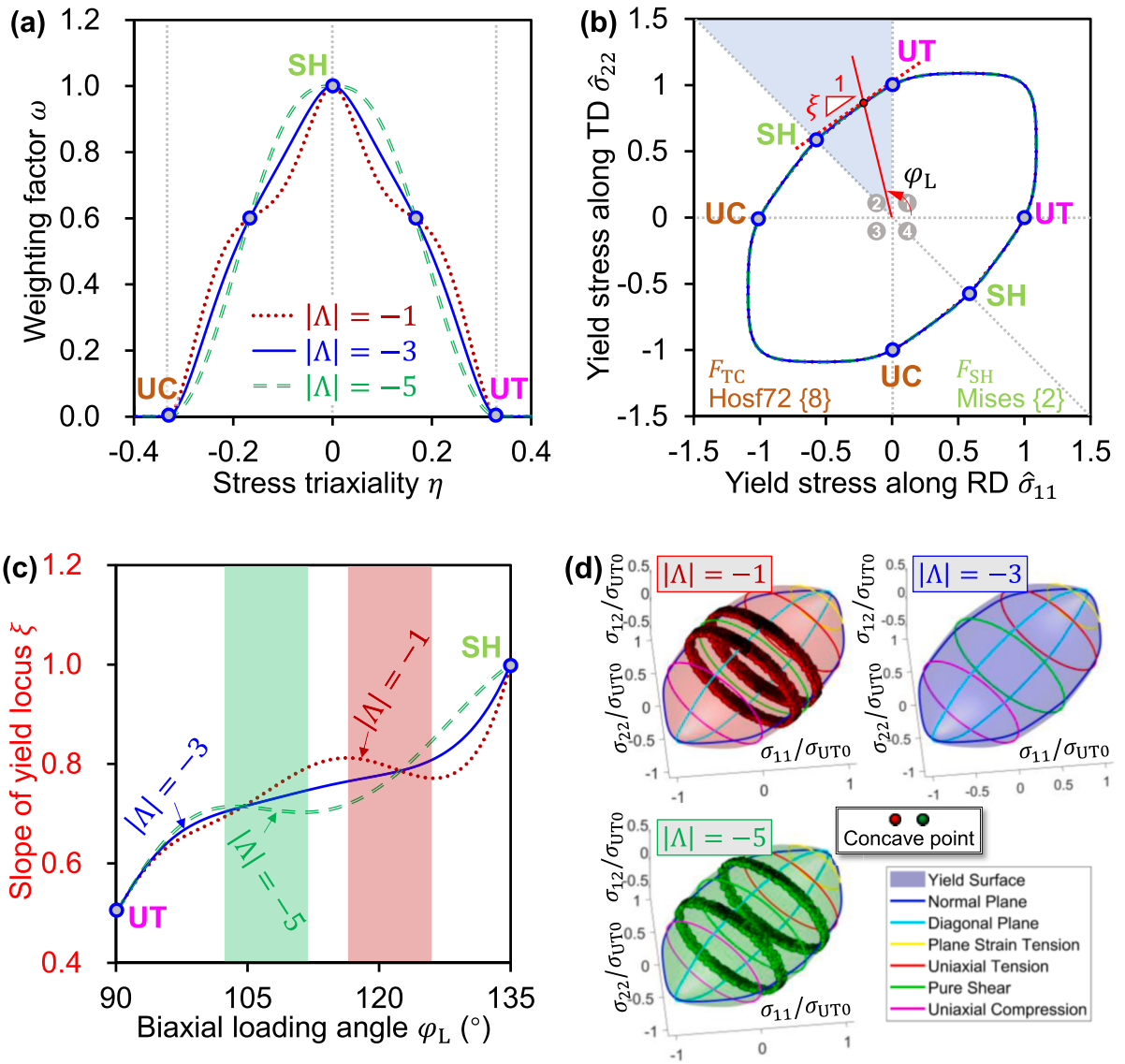

Fig. 9. Effect of Λ in the SPPoly5 governing function: (a) variation of weighting factor ω; (b) yield loci predicted by the framework employing Hosford72 with an order of 8 for TC and von Mises yield function for SH; (c) variation of the yield locus slope for biaxial loading angle ranging from 90° to 135°; (d) 3D yield surfaces with concave areas identified using the M-GINCA method.

vs. φ_L curve corresponding to $\Lambda = -3$ (blue solid curve) is continuously increasing, and the other two curves ($\Lambda = -1$ and $\Lambda = -5$) have decreasing segments in different φ_L ranges. That is to say, the sign of its curvature changes when φ_L changes from 90° to 135° Hence, both a too large Λ and a too small Λ will cause the yield locus to lose convexity in the blue shaded area in Fig. 9b. To further demonstrate the influence of Λ on the convexity of the 3D yield surface, a modified geometry-inspired numerical convex analysis (M-GINCA) method recently proposed by Du et al. (2024) was used to analyze the yield surface corresponding to the three evolutions of ω. The new M-GINCA method overcomes ambiguous identification results with the GINCA method proposed by Lou et al. (2024), providing accurate and robust convexity identification through simple geometric analysis while maintaining user-friendliness. It was found that in Fig. 9d, the yield surfaces with $\Lambda = -1$ and -5 are indeed concave under different loading conditions. In contrast, the yield surface corresponding to $\Lambda = -3$ is convex, with no concave points observed. Because the employed yield functions are isotropic, the concave band of the 3D yield surface aligns with the concave segment of the yield locus in the normal plane. Specifically, the concave band of the yield surface for $\Lambda = -1$ and -5 in Fig. 9d corresponds to the concave angle band in Fig. 9c. Hence, it is worth noting that the choice of a suitable Λ value in the SPPoly5 function plays a vital role in ensuring the convexity of the yield surface.

In conclusion, to ensure the convexity of the calculated yield surface, the following main considerations must be addressed. **(1)** It is essential that the yield function used to describe the yield surface in the first and third quadrants, denoted as $\Phi_{TC}(\boldsymbol{\sigma})$, should inherently be convex. **(2)** It is advisable to select the SPPoly5 function with an appropriate Λ to govern the relationship between ω and η. **(3)** The predicted yield surface should be checked by the M-GINCA method. In Section 6, the convexity of all yield surfaces for the real materials when using different plasticity models was validated.

6. Calibration and verification

In this section, various automotive sheet metals, including a high-strength dual-phase steel and a high-strength Al alloy are investigated to validate the proposed general framework and to provide valuable insights into the suitability of different models for different materials and loading conditions. For comparison, other existing plasticity models in the literature were considered and summarized in Table 4 to evaluate the predictive accuracy of the anisotropic plastic responses. For the non-quadratic Yld2k-2d, EYld2k-2d, STGF-Yld2k-2d-SH, and STGF-NAFR-Min16-SH yield functions, an order of 6 was selected for BCC metals, and 8 for FCC metals. The number of parameters in each yield function is also included in Table 4. The parameters of Hill48 and Poly6–18p are analytically calibrated based on the experimental data, and the detailed equations refer to the corresponding references in Table 4. For anisotropic yield functions where parameters cannot be identified analytically, various optimization algorithms can be employed to determine the anisotropic parameters (Barlat et al., 2003; Du et al., 2021; Hu et al., 2017b; Min et al., 2021). It is essential to recognize the challenges and risks associated with determining multiple parameters of the yield function through multivariable optimization (Li et al., 2016). Some algorithms (like Newton-Raphson method) may yield results that are highly sensitive to the choice of initial guess values, potentially causing the optimization process to converge to a local optimum and resulting in non-unique solutions. Numerous studies have examined strategies for selecting multivariable optimization algorithms and appropriate initial values (Bandyopadhyay et al., 2018; Rong et al., 2021; Zhang et al., 2022b). For simpler yield criteria, it is typical to use parameters derived from isotropic conditions as initial values. In contrast, for more complex yield criteria, employing multiple sets of initial guesses based on literature data for materials with similar properties (such as dual-phase steels or Al alloys) can enhance the robustness of the optimization process. To minimize the potential influence of initial guesses on the optimization results, this study implemented an advanced optimization algorithm that does not depend on the input of initial guesses, thus ensuring more consistent and reliable outcomes. Specifically, the particle swarm optimization (PSO) method (Bonyadi and Michalewicz, 2017) was utilized to minimize the error function for determining the parameters of the Yld2k-2d and EYld2k-2d models. The swarm consisted of 1000 particles, and 'fmincon' was set as the hybrid function in the PSO algorithm. The default values were set for the other swarm configurations in MATLAB. Notably, in the particle swarm algorithm, there is no need to provide an initial value for the parameters to be optimized, i.e., the first guess. The optimization range for each parameter of Yld2k-2d was set between $[0,\ 2]$, while for EYld2k-2d, it was set between $[-2,\ 2]$. The optimized parameters of Yld2k-2d and EYld2k-2d are summarized in **Appendix** (Tables A1 and A2). If not particularly emphasized, the SPPoly5 function in Eq. (45) with a specific value of Λ, i.e., $\Lambda = -3$, was used to represent the relationship between the weighting factor ω and the stress triaxiality η.

6.1. Application to high-strength dual-phase steel DP980

The experimental data of DP980 at initial yielding (EPS = 0.002) are summarized in Table 5, sourced from Hou et al. (2020). The yield stresses under EBT and PST loading conditions (along the RD and TD) were measured through biaxial tensile tests using

Table 4
The investigated plasticity models in this work.

Plasticity model	Reference	Flow rule	Num. of parameters
Hill48	Hill (1948)	AFR	3
Yld2k-2d	Barlat et al. (2003)	AFR	8
EYld2k-2d	He et al. (2022)	AFR	10
Poly6–18p	Hu et al. (2023)	AFR	18
STGF-Yld2k-2d-SH	**The present work**	AFR	10
STGF-Poly6-SH		AFR	18
STGF-NAFR-Min16-SH		NAFR	6 + 5

Table 5
Experimental data of DP980 from Hou et al. (2020).

DP980	$\widehat{\sigma}_{UT0}$	$\widehat{\sigma}_{UT15}$	$\widehat{\sigma}_{UT30}$	$\widehat{\sigma}_{UT45}$	$\widehat{\sigma}_{UT60}$	$\widehat{\sigma}_{UT75}$	$\widehat{\sigma}_{UT90}$	$\widehat{\sigma}_{EBT}$
	1.000	1.025	1.002	0.998	1.017	1.017	1.040	1.013
	$\widehat{\sigma}_{PST0}$	$\widehat{\sigma}_{PST45}$	$\widehat{\sigma}_{PST90}$	$\widehat{\sigma}_{SH0}$	$\widehat{\sigma}_{SH45}$			
	1.126	1.132	1.138	0.601	0.601			
	r_{UT0}	r_{UT15}	r_{UT30}	r_{UT45}	r_{UT60}	r_{UT75}	r_{UT90}	r_{EBT}
	0.82	0.84	0.87	0.94	0.94	0.94	0.96	0.84

laser-deposited arm-strengthened cruciform specimens (Hou et al., 2018a, b; Min et al., 2022). Note that the yield stress under PST along the DD is assumed to be the average value of the stresses along the RD and TD. The yield stresses under SH loading were measured using in-plane torsion tests (Traphöner et al., 2021).

Fig. 10a presents a comparison of the predicted yield loci using various plasticity models with the experimental yield loci of DP980 in the normal plane. Hill48 slightly underestimates the yield stress of DP980 under EBT loading, while Hill48 and EYld2k-2d overestimate the yield stress of DP980 under PST along the TD. Yld2k-2d accurately describes the yield stress of DP980 under UT, EBT, and PST loadings, but underestimates the yield stress of DP980 under SH loading along the DD. Fortunately, the three plasticity models based on the proposed general framework (i.e., STGF-Yld2k-2d-SH, STGF-Poly6-SH, and STGF-NAFR-Min16-SH) along with Poly6–18p, capture the yield locus of DP980 in the normal plane very well. The experimental and predicted yield loci of DP980 in the diagonal plane are compared in Fig. 10b. Hill48, Yld2k-2d, and EYld2k-2d slightly underestimate the yield stress under SH along the RD (SH0 in Fig. 10b). Among all the investigated plasticity models in Table 4, only Poly6–18p overestimates the yield stress under PST along the DD (PST45). The proposed general plasticity framework models (STGF-Yld2k-2d-SH, STGF-Poly6-SH, and STGF-NAFR-Min16-SH) accurately describe the yield locus of DP980 in the diagonal plane. In conclusion, only the plasticity models within the general framework are able to capture the yield stresses under various loading conditions, covering a wide range of stress states and loading directions.

The comparison between predicted anisotropic yield stresses and *r*-values of DP980 under UT loading with experimental values is presented in Fig. 11. Hill48 underestimates the yield stress of DP980 under UT along 45° to the RD, while other models accurately capture the σ_{UT45} yield stress. EYld2k-2d, Poly6–18p, and STGF-Poly6-SH provide the most accurate descriptions of anisotropy in UT yield stress. Although Yld2k-2d, STGF-Yld2k-2d-SH, and STGF-NAFR-Min16-SH produce the identical predictions of anisotropy in UT yield stress, all underestimate the UT yield stress along 60° and 75° to the RD. In Fig. 11b, EYld2k-2d fails to accurately predict the UT *r*-values of DP980, despite utilizing three *r*-values (r_{UT0}, r_{UT45}, and r_{UT90}) for parameter identification, similar to Hill48, Yld2k-2d, STGF-Yld2k-2d-SH, and STGF-NAFR-Min16-SH. Conversely, the two Poly6 function, Poly6–18p and STGF-Poly6-SH, provide very accurate descriptions of the *r*-value of DP980 under UT loading, as they employ 7 *r*-values for calibrating the anisotropic parameters.

Most importantly, Fig. 12 shows the comparison between predicted and experimental anisotropic yield stresses of DP980 under PST and SH loadings. Hill48 overpredicts the yield stress of DP980 under PST loading along the TD in Fig. 12a, while EYld2k-2d overpredicts the PST yield stress along both the RD and TD. The prediction results of Yld2k-2d, STGF-Yld2k-2d-SH, and STGF-NAFR-Min16-SH are relatively close, showing higher accuracy compared to Hill48 and EYld2k-2d. Poly6–18p accurately predicts the PST yield stresses of DP980 along the RD and TD, but it overpredicts the PST yield stress along the DD, with a relative error of + 4.4%. Overall, STGF-Poly6-SH exhibits the highest prediction accuracy for plastic anisotropy in PST yield stress of DP980. As shown in Fig. 12b, all plasticity models provide reasonably symmetric predictions of the yield stress under SH loading for DP980. Considering prediction accuracy, Yld2k-2d performs the worst, underestimating the SH yield stress of DP980 along 45° to the RD with a relative error of − 4.3%. Hill48, as a quadratic yield function, predicts the SH yield stress along 45° more accurately than Yld2k-2d. EYld2k-2d, proposed by He et al. (2022) to improve the prediction accuracy of SH yield stress, provides an accurate description of the SH yield stress of DP980 along 45°. However, it loses accuracy in predicting the SH yield stress along the RD (0°), performing worse than Hill48 (see Fig. 12b). Poly6–18p accurately describes the SH yield stress along both 0° and 45° but exhibits an unreasonable wavy pattern in the predicted planar anisotropy of the SH yield stress, which contradicts the experimental results of DP980 that show planar isotropy in SH yield stress. In comparison, the three plasticity models (STGF-Yld2k-2d-SH, STGF-Poly6-SH, and STGF-NAFR-Min16-SH) based upon the general framework developed in this work accurately capture the SH yield stress along both 0° and 45°, and the predicted variation of the SH yield stress with increasing loading direction is more reasonable compared to Poly6–18p.

In conclusion, **(1)** the three proposed models based on the STGF-YLD-SH framework provide high-fidelity predictions of plastic anisotropy in DP980 across a wide range of stress states. This includes accurately predicting the yield stress under PST and SH along different loading directions, as well as the plastic flow direction (*r*-value) under UT. The accurate description of the plastic flow direction under SH loading using STGF-YLD-SH will be further discussed in Section 7.1. **(2)** Compared with non-quadratic models like Yld2k-2d and EYld2k-2d, Hill48 serves as a quadratic function with only three parameters. Despite its simplicity, Hill48 provides a relatively accurate comprehensive prediction of the plastic anisotropy of DP980, offering the highest cost performance. This efficiency makes Hill48 a popular choice for both basic research and industrial applications in describing the plastic deformation of DP steels. **(3)** EYld2k-2d was proposed as an enhancement to Yld2k-2d for better accuracy under SH loading conditions through linear transformations. However, EYld2k-2d loses accuracy in describing the *r*-values under UT loading of DP980 compared to the original Yld2k-2d model. **(4)** Poly6–18p, the existing latest polynomial yield function designed to describe both PST and SH anisotropy, fails to accurately predict PST yield stress of DP980 along 45° (see Fig. 12a). Additionally, it exhibits an unusual variation pattern in the planar anisotropy of SH yield stress relative to the loading direction, as shown in Fig. 12b. These shortcomings are addressed in the newly proposed STGF-Poly6-SH model.

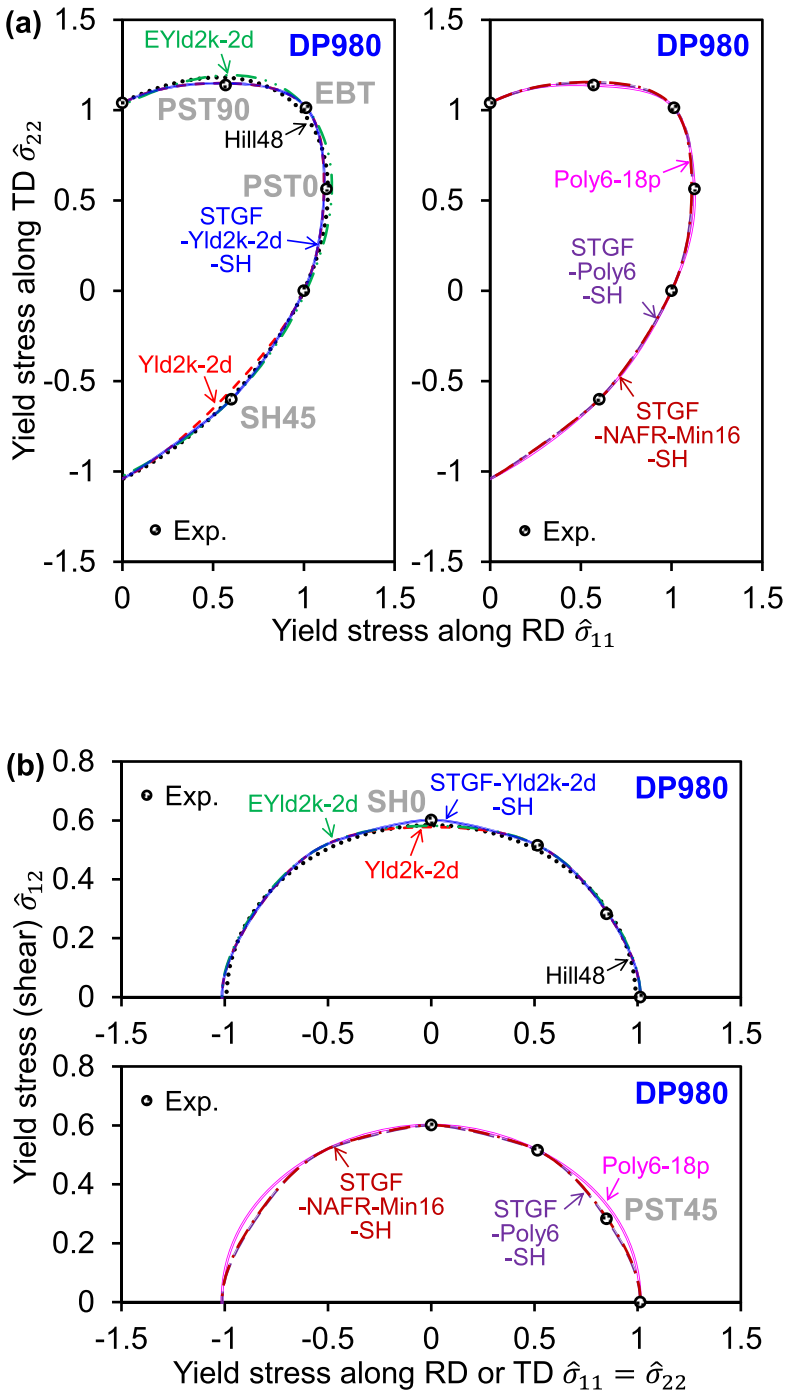

Fig. 10. Comparison of the predicted yield loci from various yield functions with experimental yield loci of DP980 in the (a) normal plane and (b) diagonal plane.

6.2. Application to high-strength Al alloy AA7075-T6

The experimental data of AA7075-T6 at initial yielding are summarized in Table 6, sourced from Rahmaan et al. (2020). Through-thickness compression tests with glued cubic specimens were performed to characterize the plastic deformation behavior of AA7075-T6 under EBT loading conditions. The mini-shear specimen geometry developed by Peirs et al. (2012) was used in the tensile tests to achieve SH deformation. Note that the PST yield stresses along three loading directions, i.e., $\hat{\sigma}_{\mathrm{PST0}}$, $\hat{\sigma}_{\mathrm{PST45}}$, and $\hat{\sigma}_{\mathrm{PST90}}$ in Table 6,

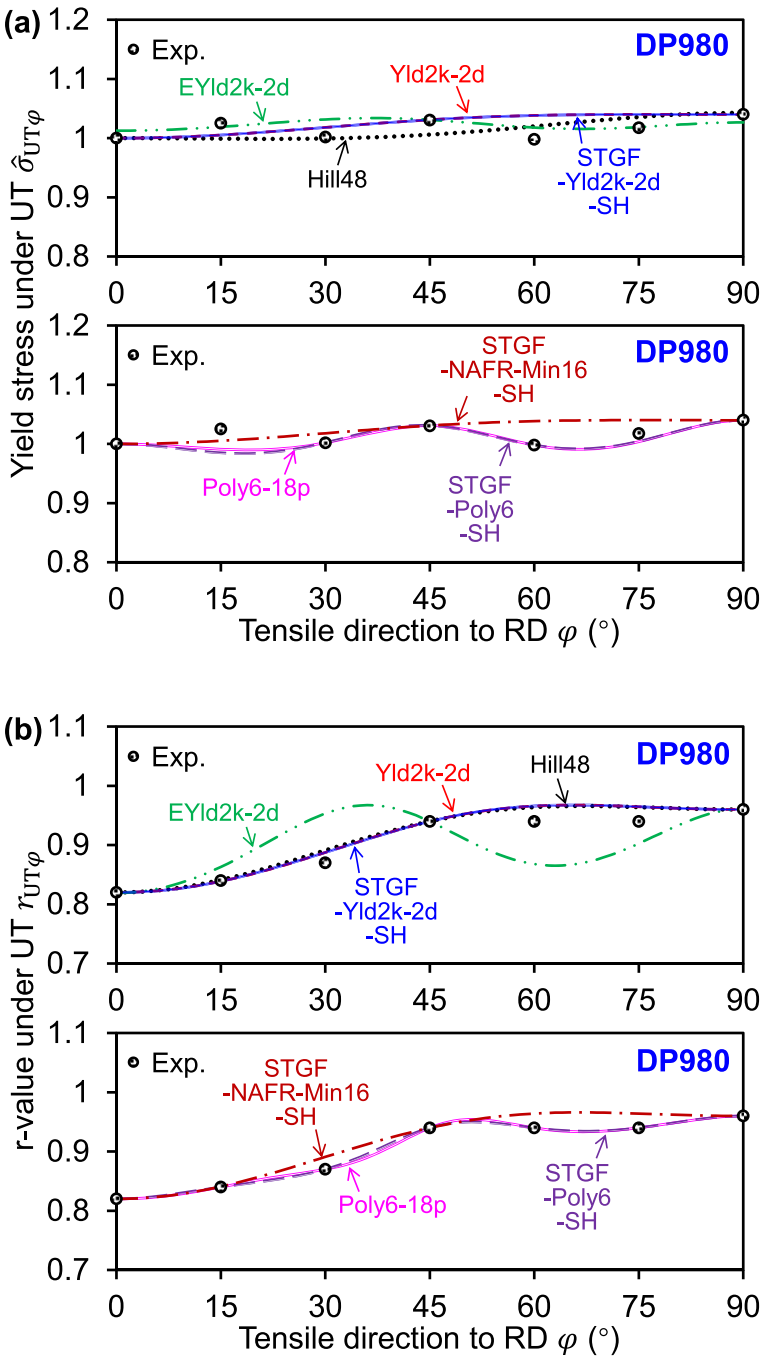

Fig. 11. (a) Yield stresses and (b) *r*-values of DP980 under UT along various angles to the RD calculated by the investigated yield functions.

predicted by the Yld2k-2d yield function, were assumed to be the experimental values of AA7075-T6 to calibrate and validate the accuracy of various plasticity models in Table 4.

Fig. 13 presents the comparison between the experimental yield locus and the calculated yield loci in the normal and diagonal planes from various plasticity models of AA7075-T6. Hill48 overpredicts the yield stress of AA7075-T6 in all three directions under PST conditions. This overprediction is an inherent shortcoming of the quadratic yield criterion when applied to Al alloys, as has been confirmed in previous studies (Hou et al., 2023c). Additionally, compared with other yield criteria, Hill48 significantly overestimates the UT yield stress of AA7075-T6 along 90°, because it does not consider the yield stress $\hat{\sigma}_{UT90}$ when calibrating parameters based on the AFR. Hill48 also overestimates the SH yield stress of AA7075-T6 along 45°, as shown in Fig. 13a. Yld2k-2d underestimates the yield stress of AA7075-T6 under SH loadings along both 0° and 45°. EYld2k-2d overestimates the PST yield stress of AA7075-T6 along 45°

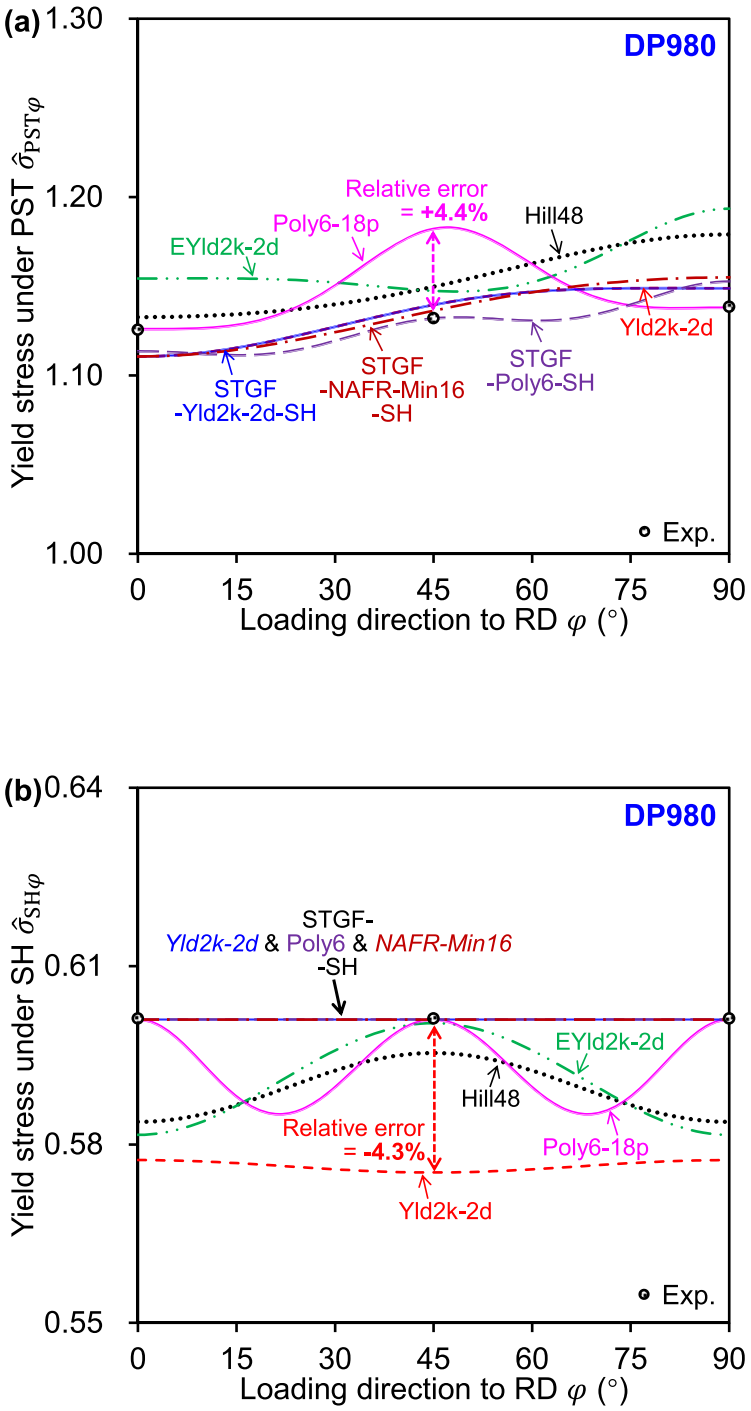

Fig. 12. Yield stresses of DP980 under (a) PST and (b) SH loadings along various angles to the RD.

and 90°, even though it employs the same order, 8, for Al alloys as Yld2k-2d. The three newly proposed plasticity models based on the STGF-YLD-SH framework and Poly6-p18 accurately describe the yield locus of AA7075-T6 in the normal plane as well as the SH yield stress along different directions. However, Poly6-p18 overestimates the PST yield stress of AA7075-T6 along 45°, as shown in Fig. 13b.

Fig. 14 compares the predictions of different plasticity models for the planer anisotropy of yield stress and *r*-value of AA7075-T6 under UT loading. It can be seen that Hill48 overestimates the UT yield stress along 60°, 75°, and 90° to the RD. The largest error occurs when predicting the 90° UT yield stress, with a relative error of +15% (see Fig. 14a). Although EYld2k-2d accurately describes the *r*-values of AA7075-T6 under UT along 0°, 45°, and 90°, it loses accuracy when predicting *r*-values along other directions, as shown in

Table 6
Experimental data of AA7075-T6 from Rahmaan et al. (2020).

AA7075-T6	$\widehat{\sigma}_{UT0}$	$\widehat{\sigma}_{UT15}$	$\widehat{\sigma}_{UT30}$	$\widehat{\sigma}_{UT45}$	$\widehat{\sigma}_{UT60}$	$\widehat{\sigma}_{UT75}$	$\widehat{\sigma}_{UT90}$	$\widehat{\sigma}_{EBT}$
	1.000	1.000	1.020	1.000	1.010	1.030	1.000	1.020
	$\widehat{\sigma}_{PST0}$	$\widehat{\sigma}_{PST45}$	$\widehat{\sigma}_{PST90}$	$\widehat{\sigma}_{SH0}$	$\widehat{\sigma}_{SH45}$			
	1.074	1.099	1.118	0.579	0.580			
	r_{UT0}	r_{UT15}	r_{UT30}	r_{UT45}	r_{UT60}	r_{UT75}	r_{UT90}	r_{EBT}
	0.67	0.70	0.75	1.00	0.85	0.94	1.13	0.71

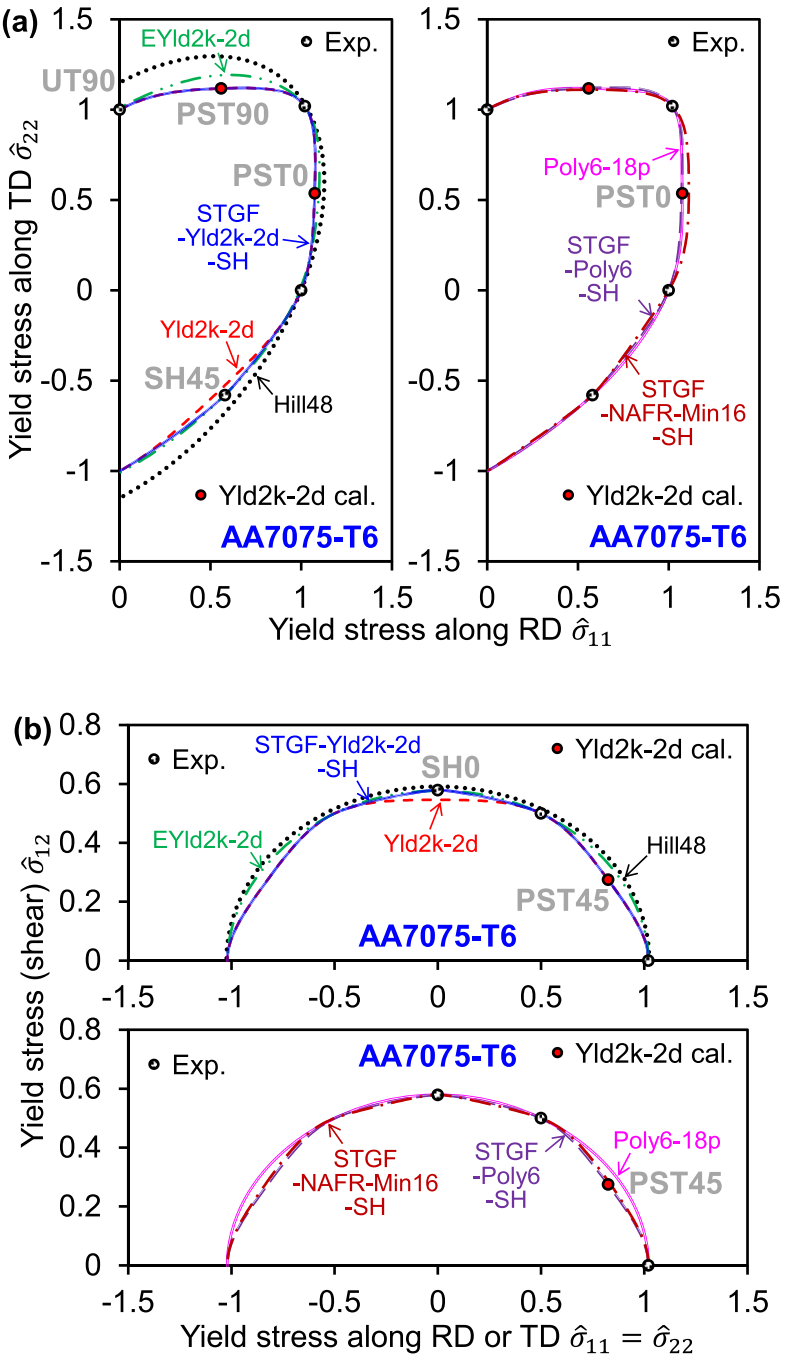

Fig. 13. Comparison of the predicted yield loci from various yield functions with experimental yield loci of AA7075-T6 in the (a) normal plane and (b) diagonal plane.

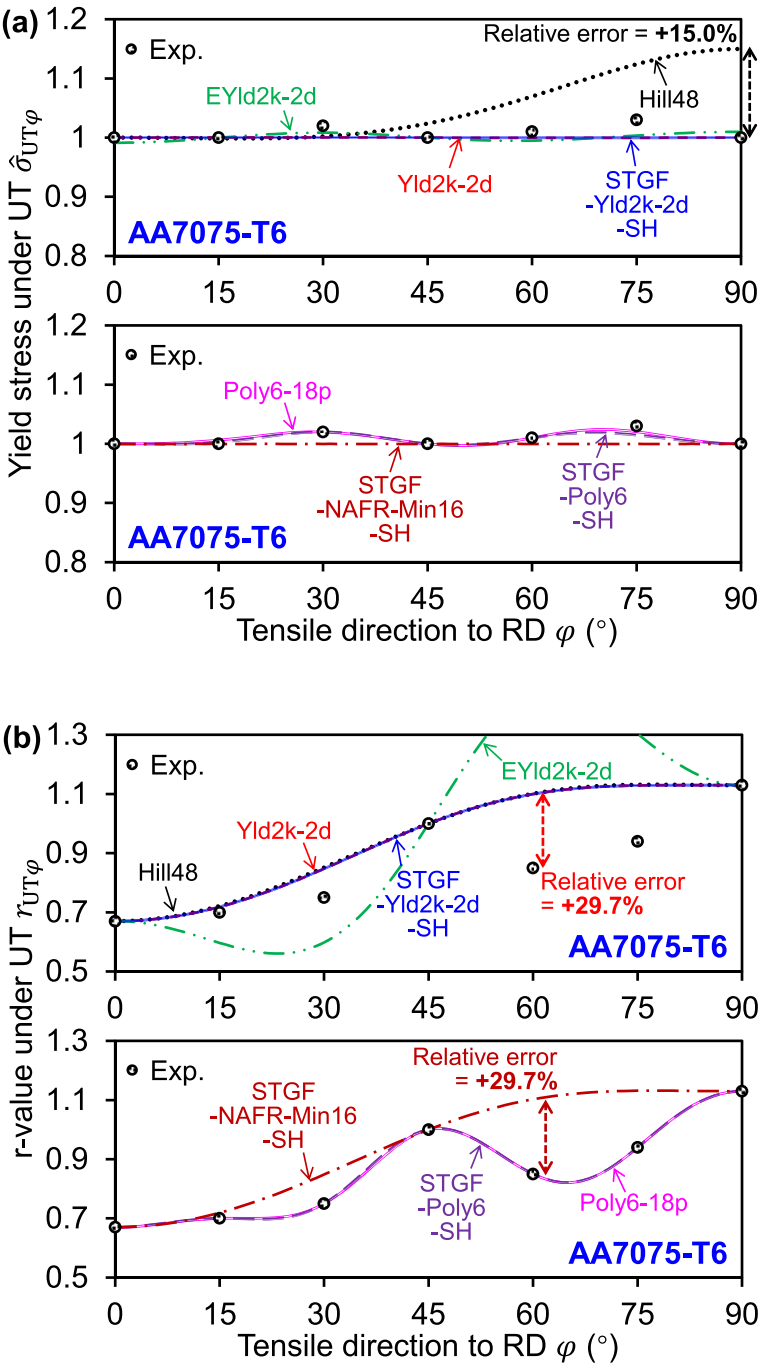

Fig. 14. (a) Yield stresses and (b) *r*-values of AA7075-T6 under UT along various angles to the RD.

Fig. 14b. This phenomenon regarding the flexible shapes of the *r*-value curve of EYld2k-2d was also reported by Hu et al. (2023) and Du et al. (2023a). The two sixth-order polynomial plasticity models, STGF-Poly6-SH and Poly6–18p, have the highest prediction accuracy for the UT yield stress and *r*-value of AA7075-T6. This is because more corresponding (UT) experimental data are used in the anisotropic parameter calibration compared to Yld2k-2d, STGF-Yld2k-2d-SH, and STGF-NAFR-Min16-SH. Note that Hill48, Yld2k-2d, STGF-Yld2k-2d-SH, and STGF-NAFR-Min16-SH show a high error when predicting the *r*-value of AA7075-T6 under UT loading along 60° and 75°, with a relative error of +29.7% along 60°.

Fig. 15 shows the comparison of experimental and predicted anisotropic yield stresses of AA7075-T6 under PST and SH states along various loading directions. Hill48 overestimates the PST yield stresses along all three directions (0°, 45°, and 90°) in Fig. 15a,

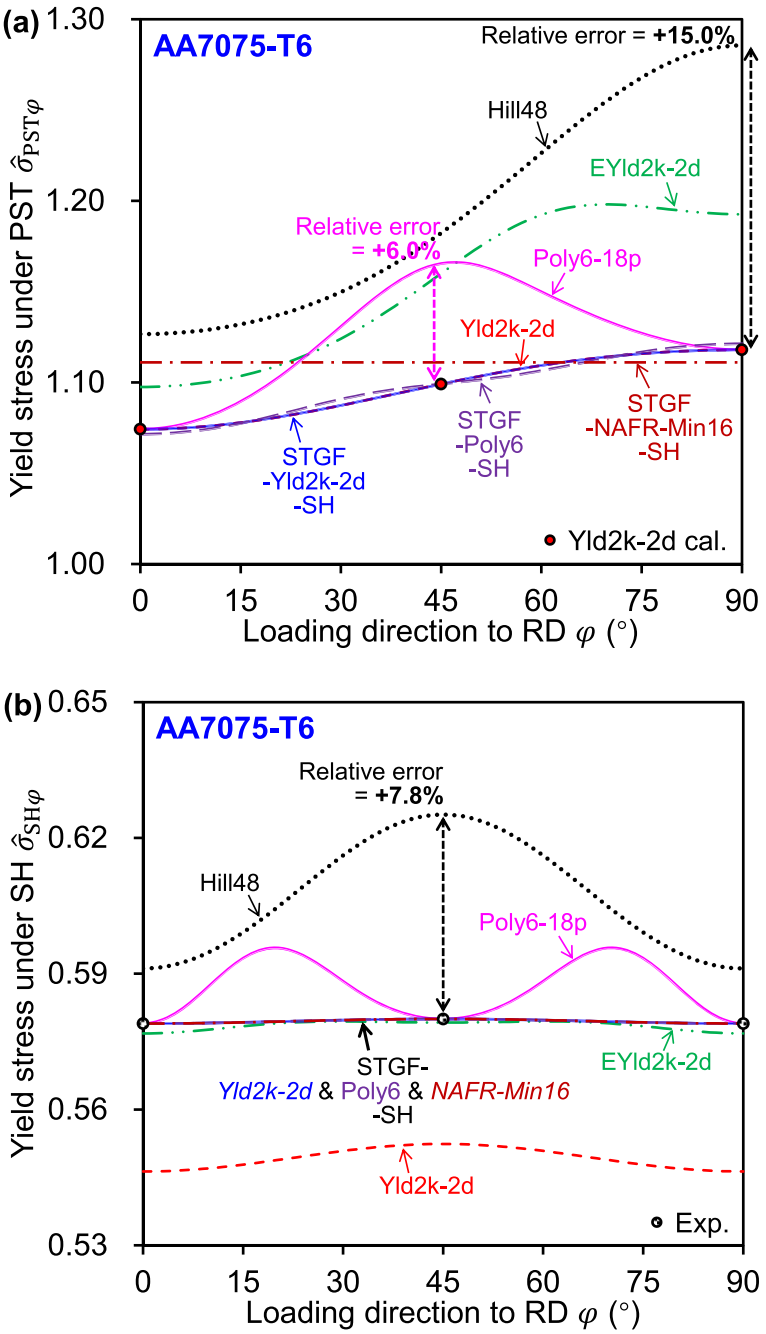

Fig. 15. Yield stresses of AA7075-T6 under (a) PST and (b) SH loadings along various angles to the RD calculated by the investigated yield functions.

consistent with the results in Fig. 13. The maximum error occurs at 90°, with a relative error of + 15.0%. EYld2k-2d overpredicts the PST yield stress along both the DD (45°) and TD (90°). STGF-NAFR-Min16-SH provides an isotropic but accurate description of the PST yield stress along 45° and 90°, but overestimates the yield stress along the RD (0°), as shown in Fig. 15a. The prediction results of Yld2k-2d, STGF-Yld2k-2d-SH, and STGF-Poly6-SH are relatively close, showing much higher accuracy compared to Hill48 and EYld2k-2d. Similar to the results of DP980, Poly6–18p accurately predicts the PST yield stresses of AA7075-T6 along the RD and TD but overpredicts the PST yield stress along the DD, with a relative error of + 6.0%. All plasticity models provide symmetric predictions of the yield stress under SH loading for AA7075-T6 in Fig. 15b. However, both Hill48 and Yld2k-2d perform poorly in terms of prediction accuracy: Hill48 overestimates the SH yield stress of AA7075-T6, with a relative error of +7.8% along 45°; while Yld2k-2d

underestimates the SH yield stress. EYld2k-2d improves the prediction accuracy of SH yield stress compared to its predecessor, Yld2k-2d. Similar to the results of DP980, Poly6–18p captures the SH yield stress along both 0° and 45° but presents an unreasonable wavy pattern in the predicted planar anisotropy of the SH yield stress. The prediction of this abnormal SH yield stress curve (magenta curve in Fig. 15b) is related to the fact that Hu et al. (2023) introduced an eighth-order polynomial to construct the Poly6–18p, which essentially increases the nonlinearity of the yield function. Comparatively speaking, the three plasticity models based upon the proposed framework (STGF-Yld2k-2d-SH, STGF-Poly6-SH, and STGF-NAFR-Min16-SH) accurately describe the SH yield stress along 0° and 45°, and the predicted variation of the SH yield stress in Fig. 15b is more reasonable than Poly6–18p. One of the most important contributions of the generalized, computationally versatile plasticity model framework is reflected here.

For a quantitative evaluation of the prediction for yield stresses and plastic flow under various stress states, the errors associated

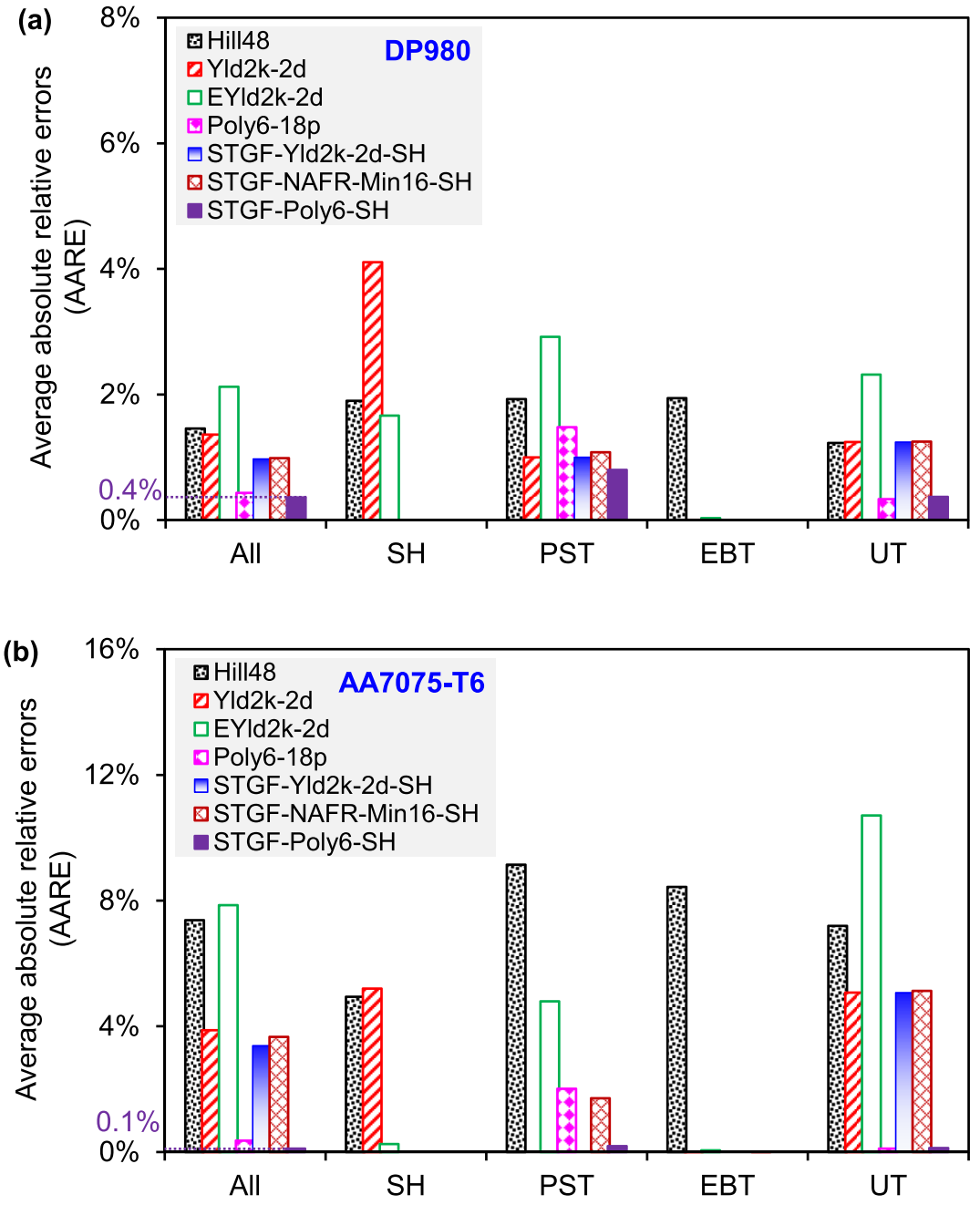

Fig. 16. AARE of predicted plastic anisotropy for (a) DP980 and (b) AA7075-T6 under various stress states. Note that the *r*-values under UT and EBT are included in the corresponding states.

with the plasticity models investigated for DP980 and AA7075-T6 are summarized in Fig. 16. The average absolute relative error (AARE) is defined in Eq. (49):

$$\mathrm{AARE} = \frac{1}{N}\sum_{i=1}^{N}\left|\frac{\mathrm{Cal}_i - \mathrm{Exp}_i}{\mathrm{Exp}_i}\right|, \tag{49}$$

where Cal_i and Exp_i are the calculated and experimental results. N is the number of data sets. For example, when comparing the predictions of plastic anisotropy under the UT state, $N = 14$, including 7 directional yield stresses and 7 directional r-values.

Some important conclusions can be drawn from Fig. 16. Firstly, as a polynomial yield function, STGF-Poly6-SH exhibits the lowest AARE among all the investigated plasticity models for predicting plastic anisotropy features across all four stress states for both DP980 and AA7075-T6, with AAREs of 0.4% and 0.1%, respectively. Despite STGF-Poly6-SH and its control group Poly6–18p having the same number (18, as summarized in Table 4) of anisotropic parameters, the overall prediction errors for both high-strength steel and high-strength Al alloy sheets are consistently lower for STGF-Poly6-SH compared to Poly6–18p. This improved accuracy is attributed to the fact that STGF-Poly6-SH, unlike Poly6–18p, can accurately predict the PST yield stress along 45° (DD), particularly for AA7075-T6, as reflected in the comparison of PST prediction accuracy in Fig. 16b. Essentially, the accurate capture of PST-DD yield stress is due to the novel and precise description of shear anisotropy developed through the STGF-YLD-SH framework, which offers greater flexibility. This framework enables the proposal of an innovative anisotropic parameter calibration strategy for the 16 parameters of Poly6 function in STGF-Poly6-SH (see Section 4.2). This analytical calibration strategy is highly valuable and should be promoted in future research on polynomial yield functions.

STGF-Yld2k-2d-SH and STGF-NAFR-Min16-SH, as representatives of non-quadratic AFR and NAFR models respectively, provide lower prediction errors than Hill48, Yld2k, and EYld2k-2d when considering comprehensive anisotropic predictions for all four stress states. The main reason for their higher accuracy compared to EYld2k-2d—evident as the prediction error of STGF-Yld2k-2d-SH for both DP980 and AA7075-T6 being around half that of EYld2k-2d—is that the prediction errors of STGF-Yld2k-2d-SH and STGF-NAFR-Min16-SH in three of the stress states (excluding EBT) are smaller than those of EYld2k-2d. Specifically, under the SH stress state, EYld2k-2d accurately predicts the yield stress only along 45°, whereas the new models can accurately capture the SH yield stress along both 0° and 45°. Furthermore, the newly proposed models, including STGF-Poly6-SH, demonstrate advantages and high flexibility in predicting directional SH yield stress, which will be discussed in detail in Section 7.2. STGF-Yld2k-2d-SH and STGF-NAFR-Min16-SH have almost the same level of prediction accuracy. However, compared to STGF-Yld2k-2d-SH, the parameters of STGF-NAFR-Min16-SH can be identified analytically without the need for optimization or interpolation. This makes it more suitable for describing the deformation-induced anisotropic hardening of metal sheets. Due to space constraints, the verification regarding anisotropic hardening features will be studied in detail in the near future.

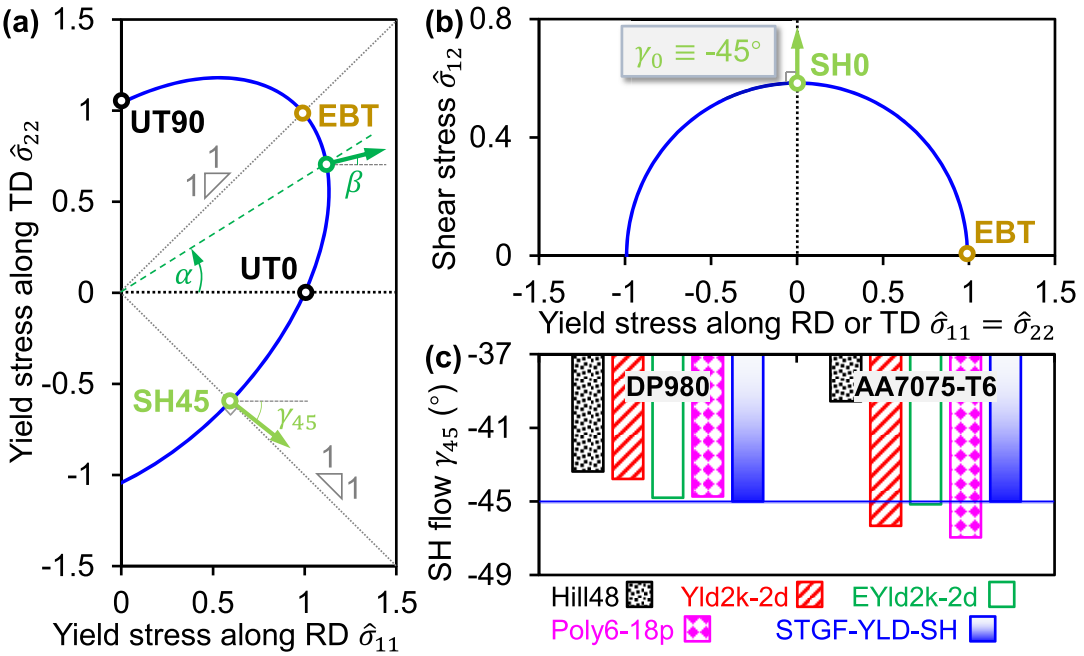

Fig. 17. (a) Yield locus and plastic flow direction β as a function of stress state angle α in the normal plane, (b) plastic flow under SH along the RD ($\gamma_0 \equiv -45°$), and (c) calculated plastic flow of DP980 and AA7075-T6 under SH along 45° to the RD using various plasticity models including Hill48, Yld2k-2d, EYld2k-2d, Poly6–18p, and the proposed STGF-YLD-SH.

EYld2k-2d loses accuracy in predicting the PST yield stress of DP980 and the directional UT r-values of both materials. Consequently, it has the largest prediction error for the plastic anisotropy of DP980 and AA7075-T6, even higher than Hill48 with only three parameters, as shown in Fig. 16. Yld2k-2d demonstrates high accuracy in predicting PST yield stress because its order (m-value in Table A1) can be adjusted for BCC and FCC microstructures. However, Yld2k-2d cannot account for the differences in the local shape of the yield locus between SH and PST loadings. This limitation leads to inherent drawbacks in predicting SH anisotropy, particularly for DP980 (Fig. 16a). Hill48 uses the r-values from three UT states to calibrate its three anisotropic parameters. Consequently, compared to other investigated plasticity models, it cannot accurately predict the yield stress and plastic flow direction (r_{EBT}) of the two materials under EBT conditions.

In comparison between the two investigated materials, the plastic anisotropy of dual-phase steel is easier to predict accurately, with the overall prediction error of all models being almost within 2%, while the prediction error for high-strength Al alloy is within 8%. As mentioned before, Hill48 and its related quadratic NAFR models (Hou et al., 2021; Li et al., 2024; Lian et al., 2018; Stoughton, 2002; Stoughton and Yoon, 2004) are widely used in describing the anisotropy of steels. When it comes to the accurate description of the plastic anisotropy of Al alloys, it is recommended to employ the non-quadratic yield functions (Hou et al., 2023c). Additionally, Al alloys generally show obvious directional characterization under UT loading (Abd El-Aty et al., 2019; Du et al., 2023b; Liu et al., 2023a), so it is recommended to adopt the newly proposed STGF-Poly6-SH model.

7. Discussion

In the previous section, the accuracy of the proposed plasticity model framework in describing the plastic anisotropy of the two metallic sheets was verified. This section will analyze and discuss its description of plastic flow and its high flexibility in predicting yield stress in SHDD.

7.1. Intrinsic shear constraint within the proposed general framework

Abedini et al. (2018) stated that some existing phenomenological yield functions lead to non-physical artifacts under SH loading. This manifests as generated through-thickness strains at zero stress triaxiality ($\sigma_1 = -\sigma_2$), indicating that the principal strain ratio deviates from -1. Fig. 17a defines the stress state angle α in the normal plane and the corresponding plastic flow direction β. The relationship between the stress ratio and stress state angle (α) is presented as follows:

$$\frac{\sigma_2}{\sigma_1} = \tan\alpha \in [-1, 1]. \tag{50}$$

Note that when $\tan\alpha = 1$, the material deforms under EBT; $\tan\alpha = 0$ corresponds to UT loading; and $\tan\alpha = -1$ corresponds to SH loading. Based on various loading directions φ relative to the RD, the stress components can be calculated using the coordinate system rotation:

$$\begin{bmatrix}\sigma_{11}\\ \sigma_{22}\\ \sigma_{12}\end{bmatrix} = \begin{bmatrix}\cos^2\varphi & \sin^2\varphi\\ \sin^2\varphi & \cos^2\varphi\\ \sin\varphi\cos\varphi & -\cos\varphi\sin\varphi\end{bmatrix}\begin{bmatrix}\sigma_1\\ \sigma_2\end{bmatrix} = \sigma_1\begin{bmatrix}\cos^2\varphi & \sin^2\varphi\\ \sin^2\varphi & \cos^2\varphi\\ \sin\varphi\cos\varphi & -\cos\varphi\sin\varphi\end{bmatrix}\begin{bmatrix}1\\ \tan\alpha\end{bmatrix}. \tag{51}$$

According to the normality rule for plastic deformation, which states that the plastic strain increment (plastic flow direction) is normal to the surface of the plastic potential for a given stress state, we have

$$\beta = \tan^{-1}\left(\frac{d\varepsilon_2}{d\varepsilon_1}\right) = \tan^{-1}\left[\left(\frac{\partial\Phi}{\partial\sigma_2}\right)\Big/\left(\frac{\partial\Phi}{\partial\sigma_1}\right)\right], \tag{52}$$

with

$$\begin{bmatrix}\dfrac{\partial\Phi}{\partial\sigma_1}\\ \dfrac{\partial\Phi}{\partial\sigma_2}\end{bmatrix} = \begin{bmatrix}\cos^2\varphi & \sin^2\varphi & \sin\varphi\cos\varphi\\ \sin^2\varphi & \cos^2\varphi & -\cos\varphi\sin\varphi\end{bmatrix}\begin{bmatrix}\dfrac{\partial\Phi}{\partial\sigma_{11}}\\ \dfrac{\partial\Phi}{\partial\sigma_{22}}\\ \dfrac{\partial\Phi}{\partial\sigma_{12}}\end{bmatrix}, \tag{53}$$

where $\Phi(\boldsymbol{\sigma})$ is the plastic potential function, which is identical to the yield stress function in the AFR plasticity models including Hill48, Yld2k-2d, EYld2k-2d, and Poly6–18p in this work.

Based on straightforward calculations or derivations rooted in the symmetry of the yield functions, it is evident that the ratio of major and minor strains is -1 when the material undergoes SH deformation along the RD (0°) for all investigated plasticity models. The material has a plastic flow direction exactly along the σ_{12} axis, as illustrated in Fig. 17b. The direction of plastic flow under SH along 45° to the RD (γ_{45}, DD), as defined in Fig. 17a, is predicted using various plasticity models and is compared in Fig. 17c. Only the proposed models based on the general framework (STGF-YLD-SH) provide accurate predictions of $\gamma_{45} = -45°$ for both DP980 and AA7075-T6, thereby preventing plastic strain in the thickness direction. EYld2k-2d can provide reasonable estimations of $\gamma_{45} = -45°$

for two materials because it imposes a constraint on SH plastic strain direction during parameter optimization, helping to prevent non-physical artifacts such as through-thickness strains under SH-DD conditions. The other investigated plasticity models fall short in accurately capturing $\gamma_{45} = -45°$, with even the recently proposed Poly6–18p significantly underestimating it for AA7075-T6. Meanwhile, Hill48 overestimates γ_{45} for AA7075-T6, resulting in a relative error of $+12.1\%$.

Fig. 18 presents the predicted evolution of the plastic flow direction β in AA7075-T6 as a function of the loading direction φ and stress state angle α. Both STGF-Poly6-SH and Poly6–18p accurately describe the plastic flow direction of AA7075-T6 under EBT loading conditions. Specifically, STGF-Poly6-SH exhibits a consistent prediction of the plastic flow direction, i.e., $\gamma = -45°$, under SH loading, irrespective of the loading direction φ, as indicated by the dashed line corresponding to $\alpha = -45°$ in Fig. 18a. This demonstrates that the SH plastic flow direction predicted by STGF-Poly6-SH ensures that no plastic strain occurs along the thickness direction when loaded under SH along any loading direction, strictly adhering to the fundamental assumption of SH deformation. However, as shown in Fig. 18b, the plastic flow direction predicted by Poly6–18p for SH deformation varies with the loading direction. This variability raises concerns about ensuring a ratio of primary and secondary strains of -1 under SH loadings, potentially leading to plastic deformation in the thickness direction.

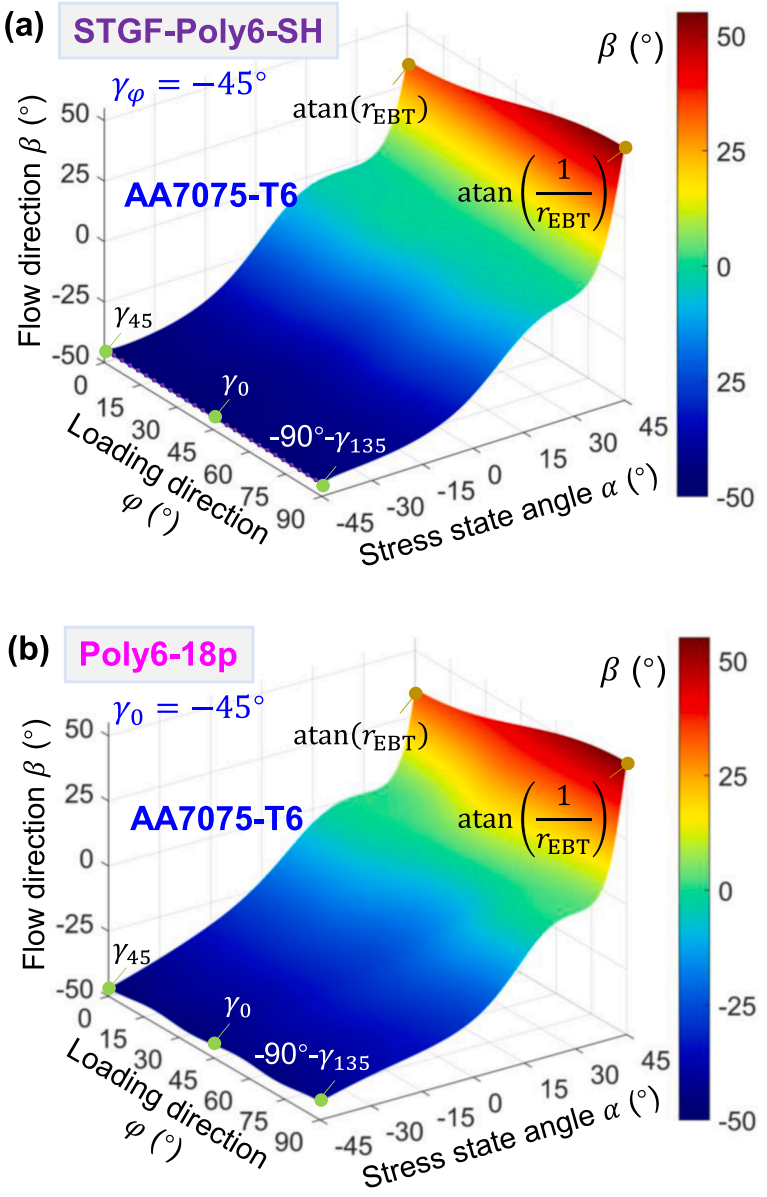

Fig. 18. Effect of loading direction φ and stress state angle α on the plastic flow direction β of AA7075-T6, calculated using (a) STGF-Poly6-SH and (b) Poly6–18p.

To focus on the description of plastic flow under SH loading, Fig. 19 presents the variation of plastic flow direction with increasing SH direction (φ) from 0° to 90° in AA7075-T6 predicted by different plasticity models. All models predict that the SH plastic flow direction is symmetrical about $\varphi = 45°$ loading, with predicted values γ_φ at 0° and 90° being $-45°$. These two special points correspond to the vertex and nadir of the 3D yield surface, respectively. Theoretically, to ensure that the principal strain ratio in the SH state is -1, the plastic flow direction for SH deformation along any direction should be $-45°$. However, as shown in Fig. 19, only the newly proposed plasticity model based on the general framework guarantees this feature, while other models fail to do so, yielding completely different prediction results. Hill48 overpredicts the direction of plastic flow under SH loading for AA7075-T6, while Yld2k-2d underestimates it. Notably, in Fig. 19c, although EYld2k-2d reasonably predicts the plastic flow direction for SH deformation along 45°, its predictions for other loading angles are poor, exhibiting a wave-shaped evolution pattern. In addition, Poly6–18p predicts more complex variations in the SH plastic flow direction with changing loading angles, as indicated by the magenta curve in Fig. 19.

In conclusion, the proposed plasticity model framework provides a more accurate prediction of the plastic flow direction under SH loading. This is attributed to the introduction of the novel function $\Phi_{SH}(\sigma)$ in Eq. (25), which describes the SH stress and plastic flow direction. Its derivatives with respect to the two principal strain components are exactly opposite (see Eq. (54)) when $\sigma_{11} = -\sigma_{22}$, corresponding to the SH condition.

$$\begin{cases} \dfrac{\partial \Phi_{SH}}{\partial \sigma_{11}} = \dfrac{2\sigma_{11} - n_1 \sigma_{22}}{2\Phi_{SH}} \\ \dfrac{\partial \Phi_{SH}}{\partial \sigma_{22}} = \dfrac{2\sigma_{22} - n_1 \sigma_{11}}{2\Phi_{SH}} \end{cases}. \tag{54}$$

Additional SH constraints, considering plastic flow, can be incorporated during the calibration procedure to eliminate non-physical artifacts observed in anisotropic yield functions such as Yld2k-2d, as studied by Abedini et al. (2018), He et al. (2022), and Zhang et al. (2022a). However, introducing constraints may lead to over-constraint in anisotropic models, potentially reducing the prediction accuracy of other anisotropic features. Fortunately, the proposed plasticity model based on STGF-YLD-SH independently describes the SH anisotropy in yield stress and exhibits an intrinsic shear constraint, thus avoiding any impact on the calibration and validation of the yield surface under other loading states.

7.2. *Flexible modeling of plastic anisotropy in shear-dominated deformation*

Section 4 introduces the novel STGF-YLD-SH framework, where a two-parameter Hill48-type function serves as the function $\Phi_{SH}(\sigma)$ in Eq. (1) to capture the shear anisotropy. Interestingly, the modeling accuracy of plastic anisotropy in SH yield stress within the STGF-YLD-SH framework can be adjusted according to various metallic sheets or different mechanical characterization methods. Table 7 lists three different options for the function $\Phi_{SH}(\sigma)$. Hill48–2p, which serves as the example in Section 4, has been verified in Section 6. Poly4–3p refers to a fourth-order polynomial yield function with three anisotropic parameters. All three options in Table 7 allow for analytic parameter identification based on the SH yield stress along three directions: σ_{SH0}, $\sigma_{SH22.5}$, and σ_{SH45}. Importantly, all three

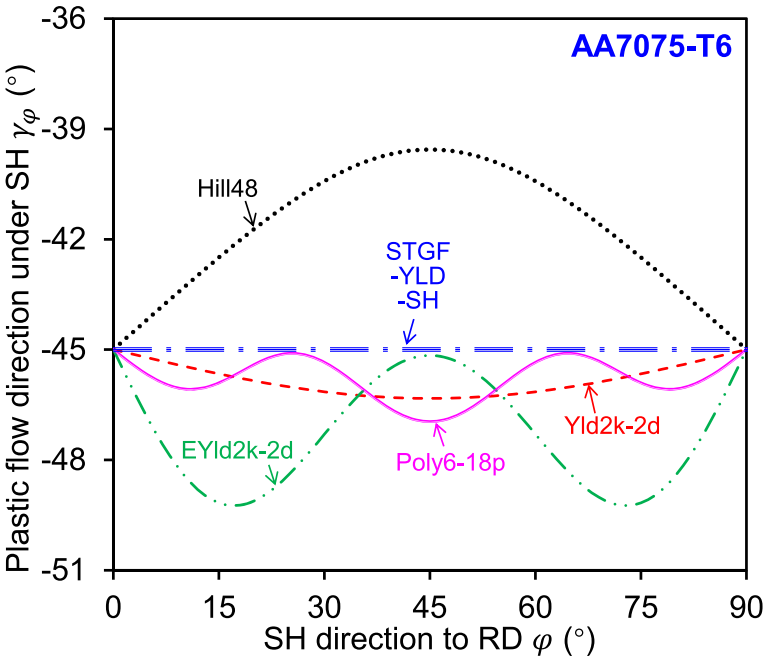

Fig. 19. Comparison of calculated plastic flow directions for AA7075-T6 under SH loading along various angles relative to the RD.

Table 7
Modeling of shear plastic anisotropy by $\Phi_{SH}(\sigma)$.

Plasticity model	Equation $\Phi_{SH}(\sigma)$	Parameter identification
Hill48–1p	$\left(\sigma_{11}^2+\sigma_{22}^2-m_1\sigma_{11}\sigma_{22}+3\sigma_{12}^2\right)^{1/2}$	$m_1=\left(\frac{\sigma_{UT0}}{\sigma_{SH45}}\right)^2-2$
Hill48–2p	$\left(\sigma_{11}^2+\sigma_{22}^2-n_1\sigma_{11}\sigma_{22}+3n_2\sigma_{12}^2\right)^{1/2}$	$\begin{cases} n_1=\left(\frac{\sigma_{UT0}}{\sigma_{SH45}}\right)^2-2 \\ n_2=\frac{1}{3}\left(\frac{\sigma_{UT0}}{\sigma_{SH0}}\right)^2 \end{cases}$
Poly4–3p	$\left(\begin{array}{c}\sigma_{11}^4-2\sigma_{11}^3\sigma_{22}+3l_1\sigma_{11}^2\sigma_{22}^2-2\sigma_{11}\sigma_{22}^3+\sigma_{22}^4 \\ +\left(6\sigma_{11}^2-6l_2\sigma_{11}\sigma_{22}+6\sigma_{22}^2\right)\sigma_{12}^2+9l_3\sigma_{12}^4\end{array}\right)^{1/4}$	$\begin{cases} l_1=\frac{1}{3}\left(\frac{\sigma_{UT0}}{\sigma_{SH45}}\right)^4-2 \\ l_2=\frac{2}{3}\left(\frac{\sigma_{UT0}}{\sigma_{SH22.5}}\right)^4-\frac{3}{2}l_3-\frac{1}{2}l_1-3 \\ l_3=\frac{1}{9}\left(\frac{\sigma_{UT0}}{\sigma_{SH0}}\right)^4 \end{cases}$

functions ensure the intrinsic shear constraint, as discussed in Section 7.1.

Fig. 20 compares the predicted yield loci under various normalized shear stress components ($\widehat{\sigma}_{12}$) with an interval of 0.05 from 0 to 0.55 for AA7075-T6, calculated using STGF-Poly6-SH with two different SH-related functions: Hill48–1p and Poly4–3p. Note that the artificial SH yield stress data assumed for AA7075-T6 are $\widehat{\sigma}_{SH0}=0.552$, $\widehat{\sigma}_{SH22.5}=0.577$, and $\widehat{\sigma}_{SH45}=0.580$, with other experimental data summarized in Table 6. There is no difference between the loci in the normal plane of these two yield surfaces in Fig. 20, because the same SH yield stress along 45° ($\widehat{\sigma}_{SH45}$) is used to calibrate the parameters of Hill48–1p and Poly4–3p $\Phi_{SH}(\sigma)$, as shown in the equations in Table 7. However, significant differences appear in the predicted yield locus at large shear stress components between Fig. 20a (Hill48–1p) and Fig. 20b (Poly4–3p).

To further investigate the differences among the three options for $\Phi_{SH}(\sigma)$ in describing the anisotropic SH yield stress, Fig. 21a shows yield loci in the SH plane, corresponding to the sections in Fig. 20 for Hill48–1p and Poly4–3p. Hill48–1p predicts a larger SH yield stress along 0° compared to Hill48–2p and Poly4–3p, which corresponds to the larger yield locus at the top ($\widehat{\sigma}_{12}$=0.55) in Fig. 20a. The predicted SH yield stress versus loading direction curves using Hill48–1p, Hill48–2p, and Poly4–3p are compared in Fig. 21b. Compared to the "Exp." data, the Poly4–3p function provides highest accuracy in capturing the planar anisotropy of SH yield stress, while Hill48–2p underestimates the SH yield stress along 22.5°, and Hill48–1p overestimates the SH yield stress along 0° to the RD of AA7075-T6.

In conclusion, the developed plasticity framework offers a novel strategy for modeling planar anisotropy in SH yield stress with both flexibility and accuracy. For materials exhibiting pronounced planar anisotropy in yielding and hardening during SHDD, a high-precision $\Phi_{SH}(\boldsymbol{\sigma})$ function, such as Poly4–3p, can be employed. Conversely, if the focus is solely on the stress state-dependent yielding and hardening behavior, a simpler function like Hill48–1p can be utilized to describe the SH stress of the material. This straightforward $\Phi_{SH}(\boldsymbol{\sigma})$ function, Hill48–1p, is particularly suitable for characterizing SH stress data obtained through in-plane torsion testing (Coppieters et al., 2022; Traphöner et al., 2021), as it measures the average response of the material subjected to SH loadings in various directions.

7.3. Simultaneous description of shear anisotropy and TCA

To simultaneously capture the shear anisotropy and TCA of advanced lightweight metallic sheets, such as quenching and partitioning (Q&P) steels, multi-weighting factors were introduced in this sub-section. The resulting and extended plasticity framework is expressed as follows:

$$\Phi(\boldsymbol{\sigma})=\omega_T\cdot\Phi_T(\boldsymbol{\sigma})+(1-\omega_T-\omega_C)\cdot\Phi_{SH}(\boldsymbol{\sigma})+\frac{\omega_C}{\widehat{\sigma}_{UC0}\left(\overline{\varepsilon}_p\right)}\cdot\Phi_C(\boldsymbol{\sigma})=\sigma_Y\left(\overline{\varepsilon}_p\right), \tag{55}$$

where $\Phi_T(\boldsymbol{\sigma})$, $\Phi_C(\boldsymbol{\sigma})$ and $\Phi_{SH}(\boldsymbol{\sigma})$ represent distinct yield functions used to separately describe the yield behavior of materials under tension, compression, and shear, respectively. $\Phi(\boldsymbol{\sigma})$ is the overall yield function. $\widehat{\sigma}_{UC0}$ denotes the normalized flow stress under UC along the RD, σ_Y is the reference flow stress under UT along the RD, and $\overline{\varepsilon}_p$ represents the equivalent plastic strain (EPS). ω_T and ω_C are two weighting factors dependent on the stress triaxiality η. Eq. (56) proposes a simple weight factor evolution law based on the piecewise trigonometric function, i.e., the SINE-type function:

$$\omega_T=\begin{cases} 0, & -\frac{2}{3}\le\eta\le 0 \quad \text{from EBC to SH} \\ \frac{1}{2}+\frac{1}{2}\sin\left(3\pi\eta-\frac{\pi}{2}\right), & 0<\eta\le\frac{1}{3} \quad \text{from SH to UT} \\ 1, & \frac{1}{3}<\eta\le\frac{2}{3} \quad \text{from UT to EBT} \end{cases}, \tag{56a}$$

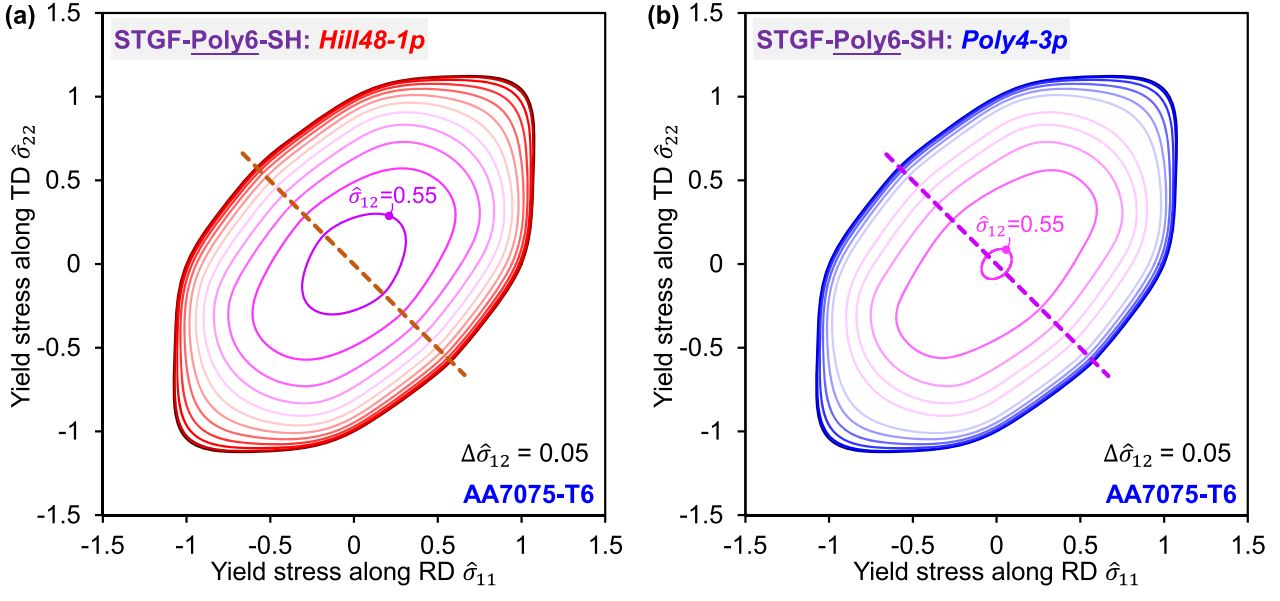

Fig. 20. Yield loci of AA7075-T6 under various normalized shear stress components from 0 to 0.5 with a 0.05 interval calculated by the STGF-Poly6-SH yield function with two different shear-dominated yield functions: (a) Hill48–1p and (b) Poly4–3p as listed in Table 7.

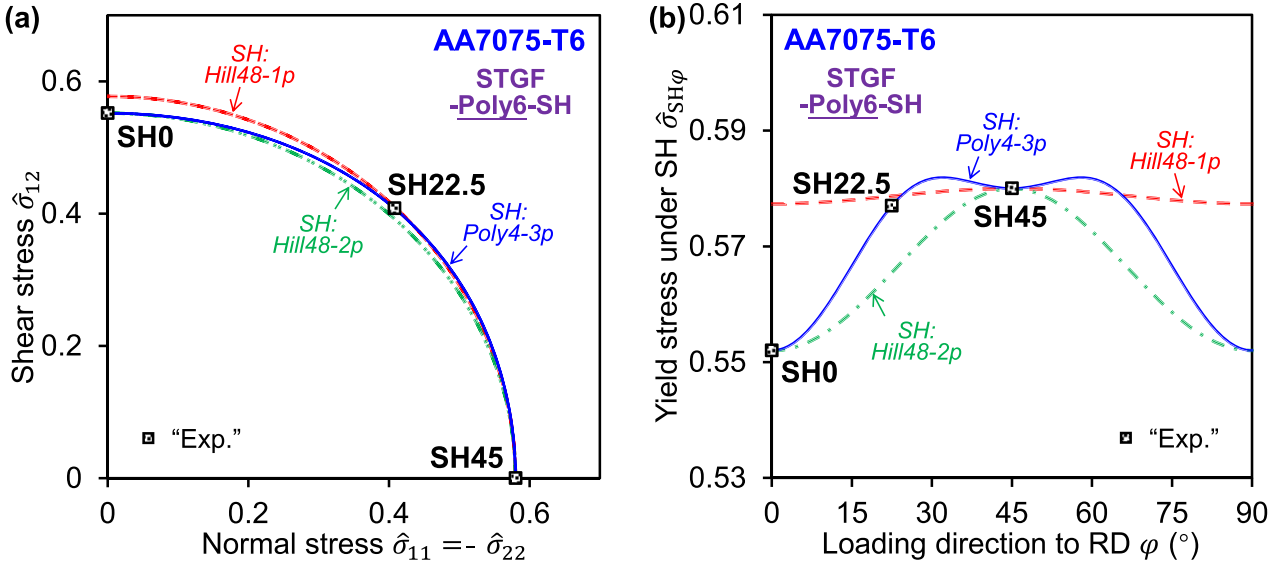

Fig. 21. Plastic anisotropy in yield stress of AA7075-T6 under SH loading calculated by the STGF-Poly6-SH yield function with three different shear-dominated yield functions, namely Hill48–1p, Hill48–2p, and Poly4–3p, as summarized in Table 7: (a) yield loci in the SH plane ($\sigma_{11} + \sigma_{22} = 0$); (b) yield stresses under SH loading along various angles to the RD.

$$\omega_C = \begin{cases} 1, & -\frac{2}{3} \le \eta \le -\frac{1}{3} \quad \text{from EBC to UC} \\ \frac{1}{2}+\frac{1}{2}\sin\left(3\pi\eta - \frac{\pi}{2}\right), & -\frac{1}{3} < \eta \le 0 \quad \text{from UC to SH} \\ 0, & 0 < \eta \le \frac{2}{3} \quad \text{from SH to EBT} \end{cases} . \tag{56b}$$

The predicted variation of the weighting factors as a function of η, according to the SINE-type function in Eq. (56) within $\eta \in [-2/3, 2/3]$, is illustrated in Fig. 22. The weighting factor for the SHDD yield function term $\Phi_{SH}(\boldsymbol{\sigma})$ is calculated as $\omega_{SH} = 1 - \omega_T - \omega_C$, and its evolution is also shown in Fig. 22, exhibiting symmetry with respect to η. To validate the extended plasticity framework in predicting shear anisotropy and TCA, experimental data of QP1180, a third-generation advanced high-strength Q&P steel, from Zhang and Lou (2023) was utilized. The flow stresses and r-values of QP1180 at a specific strain level (EPS = 0.08) are summarized in Table 8, indicating significant TCA and shear anisotropy. Note that in this case, the Poly6 yield function from Eq. (27) was employed as $\Phi_T(\boldsymbol{\sigma})$, where the stress-based Hill48 function was used for $\Phi_C(\boldsymbol{\sigma})$, and Hill48–2p from Table 7 was applied for $\Phi_{SH}(\boldsymbol{\sigma})$. Therefore, the integrated yield function can be named as STGF-Poly6-SH&TCA. All anisotropic parameters were determined analytically based on the yield stresses and r-values under various stress states listed in Table 8. For the calibration of $\Phi_T(\boldsymbol{\sigma})$ and $\Phi_{SH}(\boldsymbol{\sigma})$ functions, please refer to Section 4.2. The calibration of the stress-based Hill48 function for $\Phi_C(\boldsymbol{\sigma})$ can be found in our previous Part I paper (Hou et al., 2023a).

Fig. 23 compares the experimental yield locus with the predicted yield locus for QP1180 at EPS = 0.08, obtained using the STGF-Poly6-SH&TCA model, in both the normal and diagonal planes. The extended plasticity framework effectively captures all the yield stress pairs, accurately representing TCA features under uniaxial and biaxial loadings. To further verify the prediction accuracy of the STGF-Poly6-SH&TCA model, Fig. 24 shows the comparison of plastic anisotropy of QP1180 in yield stress under various states (UT, UC, PST, and SH), as well as the r-value under UT, against experimental results. The STGF-Poly6-SH&TCA model aligns exceptionally well with the experimental data, demonstrating its effectiveness in capturing anisotropic yield stresses of QP1180 across different stress states. Additionally, the model accurately describes the variation in plastic flow direction (r-value) with respect to the UT loading direction, as illustrated in Fig. 24b.

Considering the progress of the present model framework (STGF-YLD-SH&TCA) in balancing accuracy, parameterization, and experimental burden compared to previous models, the following key points highlight its advantages: **(1)** The STGF-Yld2k-2d-SH and STGF-Poly6-SH models, which maintain the same number of anisotropic parameters, exhibit significantly lower overall prediction errors (AARE) compared to the EYld2k-2d (He et al., 2022) and Poly6–18p (Hu et al., 2023) models, respectively. **(2)** This high level of accuracy is achieved by modeling the yield behavior across various stress states using stress triaxiality (i.e., hydrostatic pressure sensitivity) as the physical basis. This approach significantly reduces the non-linear relationship between model parameters and experimental data by coupling distinct yield functions in an additive manner. The refined calibration process enabled by this coupling ensures that the model parameters more effectively capture variations in yield stress across different stress states, ultimately enhancing the overall predictive accuracy of the model. **(3)** A major advantage of the STGF-YLD-SH&TCA framework is its precise and customizable description of SH yield (and flow) stress anisotropy. Moreover, it effectively avoids generating through-thickness strain under SH conditions, which can be problematic in other models. **(4)** While the proposed framework offers enhanced accuracy and flexibility, simpler models like Hill48 (Hill, 1948) or isotropic yield criteria (Cazacu, 2018) might be sufficient for traditional materials

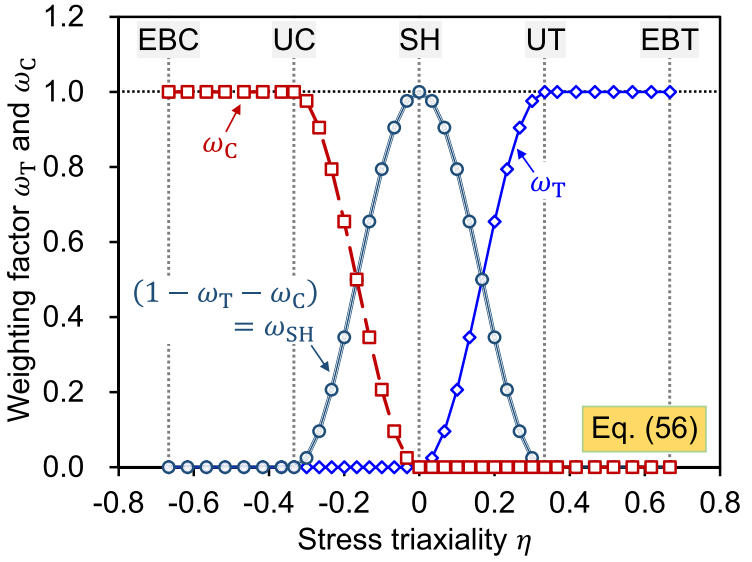

Fig. 22. Variation of weighting factor ω_T and ω_C as functions of stress triaxiality η in the SINE-type governing function.

Table 8
Experimental data of QP1180 from Zhang and Lou (2023).

QP1180									
EPS = 0.08	$\widehat{\sigma}_{UT0}$	$\widehat{\sigma}_{UT15}$*	$\widehat{\sigma}_{UT30}$*	$\widehat{\sigma}_{UT45}$	$\widehat{\sigma}_{UT60}$*	$\widehat{\sigma}_{UT75}$*	$\widehat{\sigma}_{UT90}$	$\widehat{\sigma}_{EBT}$	
	1.000	0.997	0.991	0.987	0.999	0.996	0.999	1.046	
	$\widehat{\sigma}_{UC0}$	$\widehat{\sigma}_{UC45}$	$\widehat{\sigma}_{UC90}$	$\widehat{\sigma}_{EBC}$#	$\widehat{\sigma}_{PST0}$	$\widehat{\sigma}_{PST45}$	$\widehat{\sigma}_{PST90}$	$\widehat{\sigma}_{SH0}$	$\widehat{\sigma}_{SH45}$
	0.980	0.977	0.998	0.983	1.142	1.146	1.153	0.573	0.577
	r_{UT0}	r_{UT15}*	r_{UT30}*	r_{UT45}	r_{UT60}*	r_{UT75}*	r_{UT90}	r_{EBT}#	
	0.860	0.877	0.913	0.940	0.943	0.929	0.920	0.915	

* $x_{UT\varphi} = x_{UT0} \cdot \cos^4\varphi + (4 \cdot x_{UT45} - x_{UT0} - x_{UT90}) \cdot \cos^2\varphi \cdot \sin^2\varphi + x_{UT90} \cdot \sin^4\varphi,\ x = \widehat{\sigma}$ or r.
\# $y_{EBT.C} = (y_{UT.C0} + 2 \cdot y_{UT.C45} + y_{UT.C90})/4,\ y = \widehat{\sigma}$ or r.

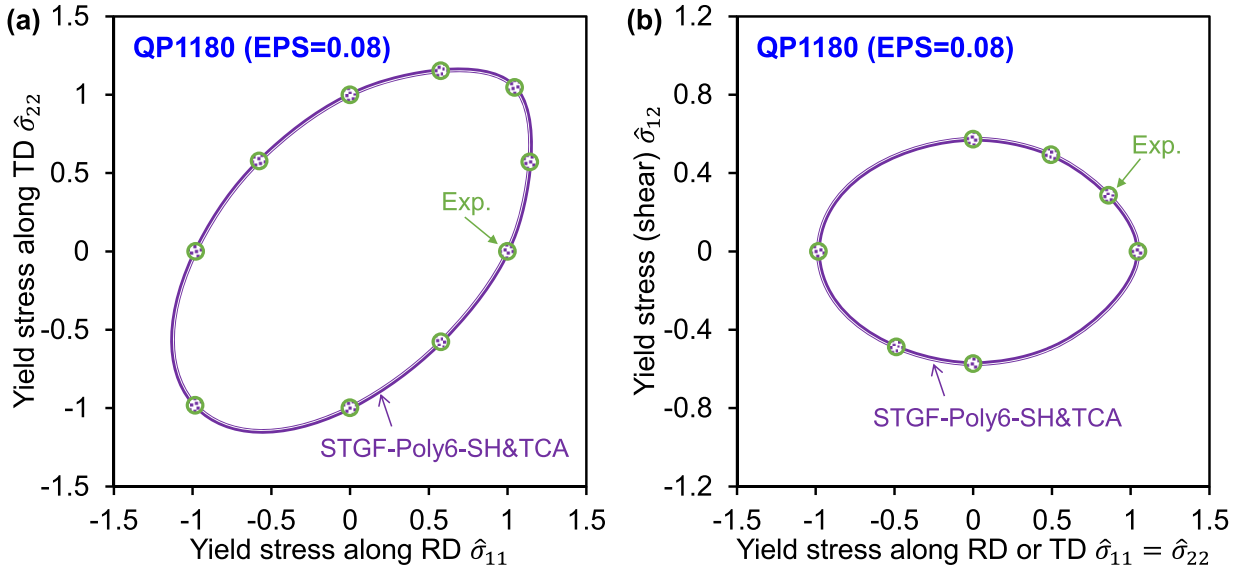

Fig. 23. Yield loci of QP1180 predicted by the proposed STGF-Poly6-SH&TCA model in (a) the normal plane and (b) the diagonal plane.

such as low-carbon steel. These simpler models can be seamlessly integrated into the proposed framework, allowing users to opt for higher precision or lower experimental cost depending on their requirements. **(5)** The primary target applications of this framework involve stress and strain analysis, as well as the precise prediction of component geometry deviations, particularly in manufacturing processes where significant amounts of SHDD occur, such as in the automotive and aerospace industries. The high precision achieved by this novel framework is particularly valuable in the realm of digital twin technology, where accurate material behavior predictions are essential for applications requiring high fidelity and reliability.

8. Summary and conclusions

A generalized, computationally versatile plasticity model framework was developed to simulate the complex plasticity behavior, particularly focusing on the plastic anisotropy of SHDD in sheet metallic materials. The main conclusions of the present work are summarized below:

(1) A stress triaxiality-dependent weighting factor is introduced to combine two anisotropic yield functions additively. One function describes yield behavior under tension, while the other addresses SHDD. The key advantage of this framework (STGF-YLD-SH) is the independent calibration of two yield functions.
(2) The STGF-YLD-SH framework was applied to existing anisotropic yield functions and flow rules, such as Yld2k-2d and Poly6 under the AFR as well as Min2016 under the NAFR.
(3) The effect of the stress triaxiality-dependent weighting factor on the shape and convexity of yield surface was elucidated. Comparative analysis suggests adopting the symmetric piecewise Poly5 function to describe the variation of the weighting factor, achieving a convex yield surface.
(4) The STGF-YLD-SH framework was validated using experimental data of two automotive sheet metals DP980 and AA7075-T6. Especially the framework naturally prevents non-physical artifacts such as through-thickness strains under SH condition. The framework allows for flexible modeling of plastic anisotropy in SH yield stress by using different SH yield functions.

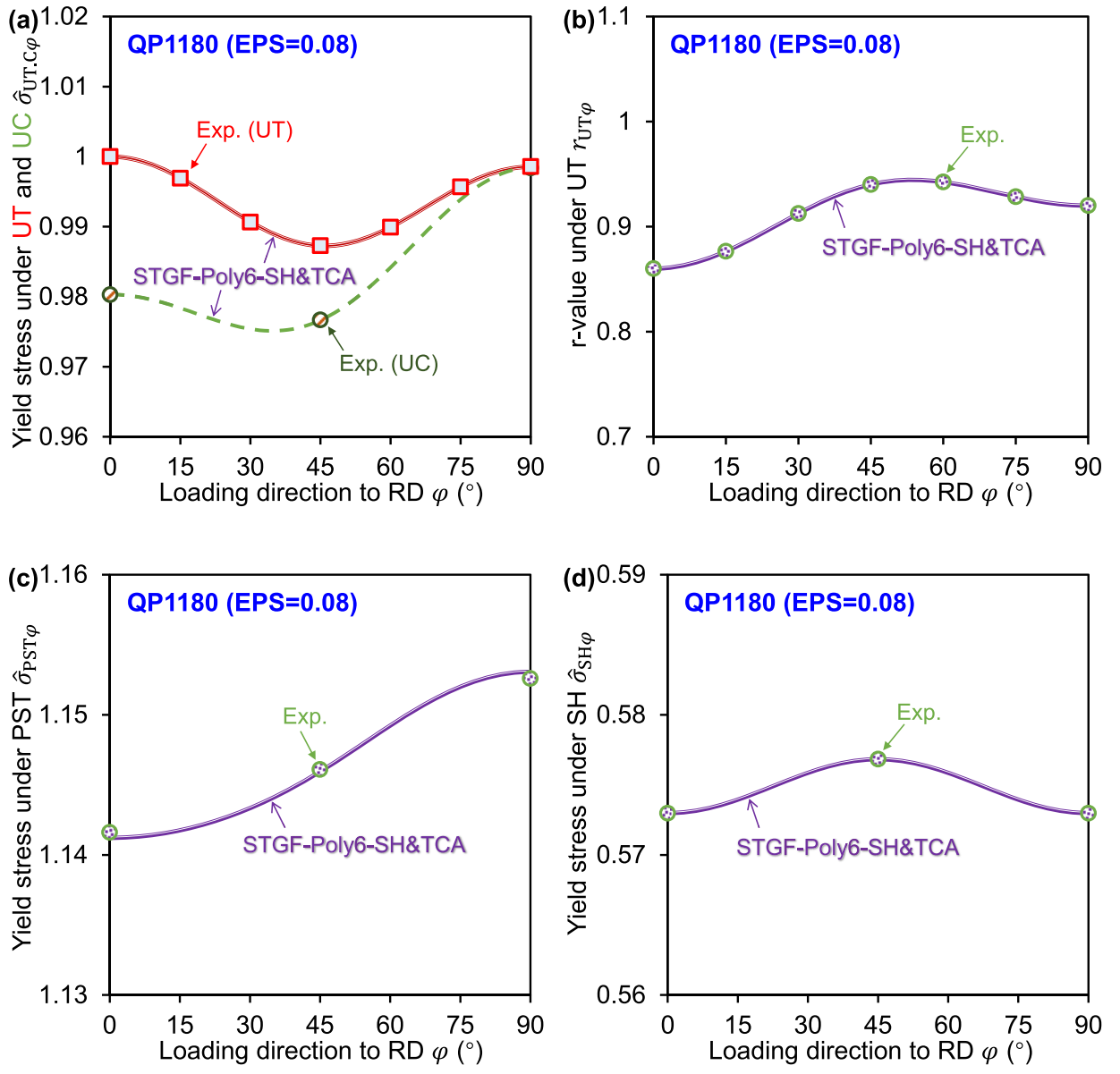

Fig. 24. Plastic anisotropy of QP1180 in (a) yield stress under UT and UC, (b) *r*-value under UT, (c) yield stress under PST, and (d) SH conditions predicted by the STGF-Poly6-SH&TCA model.

(5) The proposed framework was further extended to capture shear anisotropy and TCA simultaneously through employing two weighting factors, namely STGF-YLD-SH&TCA. The robustness of this approach has been thoroughly verified using experimental data of the QP1180 steel.

CRediT authorship contribution statement

Yong Hou: Writing – review & editing, Writing – original draft, Visualization, Funding acquisition, Conceptualization. **Junying Min:** Writing – review & editing, Investigation. **Hyung-Rim Lee:** Visualization, Writing – review & editing. **Jinjin Ha:** Writing – review & editing, Investigation. **Namsu Park:** Writing – review & editing, Investigation, Funding acquisition. **Myoung-Gyu Lee:** Writing – review & editing, Project administration.

Declaration of competing interest

The authors declare that they have no known competing financial interests or personal relationships that could have appeared to influence the work reported in this paper.

Acknowledgments

YH would like to thank the generous support from Alexander von Humboldt Foundation who awarded him a research fellowship at TU Dortmund University. NP appreciates the support from the Korea Institute of Industrial Technology as part of the development of root technology for multi-product flexible production (KITECH EO-24-0009). MGL appreciates the grant from NRF (No. 2022R1A2C2009315) and KEIT (Project No. 20010453). The authors thank the reviewers for their constructive comments which improve the technical contents of the paper.

Appendix: Identified parameters of Yld2k-2d and EYld2k-2d

Table A1
The calibrated parameters of Yld2k-2d for various materials.

Material	α_1	α_2	α_3	α_4	α_5	α_6	α_7	α_8	m
DP980	1.013	0.926	0.987	0.973	1.006	0.978	0.967	0.958	6
AA7075-T6	0.910	1.061	0.931	0.974	1.015	0.966	0.997	1.026	8

Table A2
The calibrated parameters of EYld2k-2d for various materials.

Material	c'_{11}	c'_{12}	c'_{21}	c'_{22}	c'_{66}	c''_{11}	c''_{12}	c''_{21}	c''_{22}	c''_{66}	m
DP980	1.010	-0.153	-0.006	0.806	1.074	-0.363	0.712	1.104	0.507	1.018	6
AA7075-T6	0.419	-0.546	0.493	1.214	0.966	-1.523	0.198	1.836	0.381	1.685	8

Data availability

Data will be made available on request.

References

Abd El-Aty, A., Xu, Y., Zhang, S.-H., Ha, S., Ma, Y., Chen, D., 2019. Impact of high strain rate deformation on the mechanical behavior, fracture mechanisms and anisotropic response of 2060 Al-Cu-Li alloy. J. Adv. Res. 18, 19–37. https://doi.org/10.1016/j.jare.2019.01.012.

Abedini, A., Butcher, C., Rahmaan, T., Worswick, M.J., 2018. Evaluation and calibration of anisotropic yield criteria in shear loading: constraints to eliminate numerical artefacts. Int. J. Solids Struct. 151, 118–134. https://doi.org/10.1016/j.ijsolstr.2017.06.029.

Bai, Y., Wierzbicki, T., 2008. A new model of metal plasticity and fracture with pressure and lode dependence. Int. J. Plast. 24, 1071–1096. https://doi.org/10.1016/j.ijplas.2007.09.004.

Banabic, D., Kuwabara, T., Balan, T., Comsa, D., Julean, D., 2003. Non-quadratic yield criterion for orthotropic sheet metals under plane-stress conditions. Int. J. Mech. Sci. 45, 797–811. https://doi.org/10.1016/S0020-7403(03)00139-5.

Bandyopadhyay, K., Hariharan, K., Lee, M.-G., Zhang, Q., 2018. Robust multi objective optimization of anisotropic yield function coefficients. Mater. Des. 156, 184–197. https://doi.org/10.1016/j.matdes.2018.06.033.

Baral, M., Ripley, P.W., Lou, Y., Korkolis, Y.P., 2024. Anisotropic ductile fracture of a stainless steel under biaxial loading: experiments and predictions. Int. J. Plast. 175, 103927. https://doi.org/10.1016/j.ijplas.2024.103927.

Barlat, F., Aretz, H., Yoon, J.W., Karabin, M.E., Brem, J.C., Dick, R.E., 2005. Linear transfomation-based anisotropic yield functions. Int. J. Plast. 21, 1009–1039. https://doi.org/10.1016/j.ijplas.2004.06.004.

Barlat, F., Becker, R.C., Hayashida, Y., Maeda, Y., Yanagawa, M., Chung, K., Brem, J.C., Lege, D.J., Matsui, K., Murtha, S.J., Hattori, S., 1997. Yielding description for solution strengthened aluminum alloys. Int. J. Plast. 13, 385–401. https://doi.org/10.1016/S0749-6419(97)80005-8.

Barlat, F., Brem, J.C., Yoon, J.W., Chung, K., Dick, R.E., Lege, D.J., Pourgoghrat, F., Choi, S.H., Chu, E., 2003. Plane stress yield function for aluminum alloy sheets - part 1: theory. Int. J. Plast. 19, 1297–1319. https://doi.org/10.1016/S0749-6419(02)00019-0.

Barlat, F., Gracio, J.J., Lee, M.G., Rauch, E.F., Vincze, G., 2011. An alternative to kinematic hardening in classical plasticity. Int. J. Plast. 27, 1309–1327. https://doi.org/10.1016/j.ijplas.2011.03.003.

Barlat, F., Ha, J.J., Gracio, J.J., Lee, M.G., Rauch, E.F., Vincze, G., 2013. Extension of homogeneous anisotropic hardening model to cross-loading with latent effects. Int. J. Plast. 46, 130–142. https://doi.org/10.1016/j.ijplas.2012.07.002.

Barlat, F., Lege, D.J., Brem, J.C., 1991. A six-component yield function for anisotropic materials. Int. J. Plast. 7, 693–712. https://doi.org/10.1016/0749-6419(91)90052-Z.

Barlat, F., Lian, J., 1989. Plastic behavior and stretchability of sheet metals .1. A yield function for orthotropic sheets under plane-stress conditions. Int. J. Plast. 5, 51–66. https://doi.org/10.1016/0749-6419(89)90019-3.

Barlat, F., Yoon, J.W., Cazacu, O., 2007. On linear transformations of stress tensors for the description of plastic anisotropy. Int. J. Plast. 23, 876–896. https://doi.org/10.1016/j.ijplas.2006.10.001.

Barlat, F., Yoon, S.Y., Lee, S.Y., Wi, M.S., Kim, J.H., 2020. Distortional plasticity framework with application to advanced high strength steel. Int. J. Solids Struct. 202, 947–962. https://doi.org/10.1016/j.ijsolstr.2020.05.014.

Bassani, J.L., 1977. Yield characterization of metals with transversely isotropic plastic properties. Int. J. Mech. Sci. 19, 651–660. https://doi.org/10.1016/0020-7403(77)90070-4.
Bonyadi, M.R., Michalewicz, Z., 2017. Particle swarm optimization for single objective continuous space problems: a review. Evol. Comput. 25, 1–54. https://doi.org/10.1162/EVCO_r_00180.
Boogaard, A.H.v.d., 2002. Thermally enhanced forming of aluminium sheet. Modelling and Experiments. Faculty of Engineering Technology. University of Twente, Ponsen & Looijen. https://ris.utwente.nl/ws/portalfiles/portal/6073518/boogaardthesis.pdf.
Brosius, A., Küsters, N., Lenzen, M., 2018. New method for stress determination based on digital image correlation data. CIRP Ann. 67, 269–272. https://doi.org/10.1016/j.cirp.2018.04.026.
Budiansky, B., 1984. Anisotropic plasticity of plane-isotropic sheets. In: Dvorak, G.J., Shield, R.T. (Eds.), Studies in Applied Mechanics. Elsevier, pp. 15–29. https://doi.org/10.1016/B978-0-444-42169-2.50008-5.
Cazacu, O., 2018. New yield criteria for isotropic and textured metallic materials. Int. J. Solids Struct. 139, 200–210. https://doi.org/10.1016/j.ijsolstr.2018.01.036.
Cazacu, O., Barlat, F., 2004. A criterion for description of anisotropy and yield differential effects in pressure-insensitive metals. Int. J. Plast. 20, 2027–2045. https://doi.org/10.1016/j.ijplas.2003.11.021.
Cazacu, O., Plunkett, B., Barlat, F., 2006. Orthotropic yield criterion for hexagonal closed packed metals. Int. J. Plast. 22, 1171–1194. https://doi.org/10.1016/j.ijplas.2005.06.001.
Choi, H., Yoon, J.W., 2019. Stress integration-based on finite difference method and its application for anisotropic plasticity and distortional hardening under associated and non-associated flow rules. Comput. Methods Appl. Mech. Eng. 345, 123–160. https://doi.org/10.1016/j.cma.2018.10.031.
Coppieters, S., Traphöner, H., Stiebert, F., Balan, T., Kuwabara, T., Tekkaya, A.E., 2022. Large strain flow curve identification for sheet metal. J. Mater. Process. Technol. 117725. https://doi.org/10.1016/j.jmatprotec.2022.117725.
Dick, C.P., Korkolis, Y.P., 2015. Anisotropy of thin-walled tubes by a new method of combined tension and shear loading. Int. J. Plast. 71, 87–112. https://doi.org/10.1016/j.ijplas.2015.04.006.
Drucker, D.C., 1949. Relation of experiments to mathematical theories of plasticity. J. Appl. Mech. 16, 349–357. https://doi.org/10.1115/1.4010009.
Du, K., Dong, L., Zhang, H., Mu, Z., Dong, H., Wang, H., Ren, Y., Sun, L., Zhang, L., Yuan, X., 2023a. Modeling of Eyld2000-2d anisotropic yield criterion considering strength differential effect and analysis of optimal calibration strategy. Materials (Basel) 16, 6445. https://doi.org/10.3390/ma16196445.
Du, K., Huang, S., Hou, Y., Wang, H., Wang, Y., Zheng, W., Yuan, X., 2023b. Characterization of the asymmetric evolving yield and flow of 6016-T4 aluminum alloy and DP490 steel. J. Mater. Sci. Technol. 133, 209–229. https://doi.org/10.1016/j.jmst.2022.05.040.
Du, K., Huang, S.H., Li, X.Q., Wang, H.B., Zheng, W.T., Yuan, X.G., 2022. Evolution of yield behavior for AA6016-T4 and DP490—towards a systematic evaluation strategy for material models. Int. J. Plast. 154, 103302. https://doi.org/10.1016/j.ijplas.2022.103302.
Du, K., Huang, S.H., Shi, M.H., Li, L.J., Huang, H.J., Zhang, S.J., Zheng, W.T., Yuan, X.G., 2021. Effects of biaxial tensile mechanical properties and non-integer exponent on description accuracy of anisotropic yield behavior. Mater. Des. 212, 110210. https://doi.org/10.1016/j.matdes.2021.110210.
Du, K., Ren, Y., Hou, Y., Yang, Y., Li, X., Wang, Z., Zheng, W., Yuan, X., 2024. Analytical symmetric/asymmetric anisotropic yield criteria covering wider stress states under non-associated flow rule and a geometric convexity proof method: modeling and validation. Int. J. Plast. Under review.
Ferron, G., Makkouk, R., Morreale, J., 1994. A parametric description of orthotropic plasticity in metal sheets. Int. J. Plast. 10, 431–449. https://doi.org/10.1016/0749-6419(94)90008-6.
Fuhg, J.N., Fau, A., Bouklas, N., Marino, M., 2023. Enhancing phenomenological yield functions with data: challenges and opportunities. Eur. J. Mech. A. Solids 99, 104925. https://doi.org/10.1016/j.euromechsol.2023.104925.
Grolleau, V., Roth, C.C., Mohr, D., 2022. Design of in-plane torsion experiment to characterize anisotropic plasticity and fracture under simple shear. Int. J. Solids Struct. https://doi.org/10.1016/j.ijsolstr.2021.111341.
Han, G., He, J., Li, S., 2022. Simple shear deformation of sheet metals: finite strain perturbation analysis and high-resolution quasi-in-situ strain measurement. Int. J. Plast. 103194. https://doi.org/10.1016/j.ijplas.2021.103194.
Han, G., He, J., Li, S., Lin, Z., 2024. Simple shear methodology for local structure–property relationships of sheet metals: state-of-the-art and open issues. Prog. Mater Sci. 143, 101266. https://doi.org/10.1016/j.pmatsci.2024.101266.
Hao, S., Dong, X., 2020. Interpolation-based plane stress anisotropic yield models. Int. J. Mech. Sci. 178, 105612. https://doi.org/10.1016/j.ijmecsci.2020.105612.
He, Z., Zhang, K., Zhu, H., Lin, Y., Fu, M.W., Yuan, S., 2022. An anisotropic constitutive model for forming of aluminum tubes under both biaxial tension and pure shear stress states. Int. J. Plast. 152, 103259. https://doi.org/10.1016/j.ijplas.2022.103259.
Hill, R., 1948. A theory of the yielding and plastic flow of anisotropic metals. Proc. R. Soc. Lond. 193, 281–297. https://doi.org/10.1098/rspa.1948.0045. Series A. Mathematical and Physical Sciences.
Hill, R., 1979. Theoretical plasticity of textured aggregates. In: Proceedings of the Mathematical Proceedings of the Cambridge Philosophical Society. Cambridge University Press, pp. 179–191. https://doi.org/10.1017/S0305004100055596.
Hill, R., 1990. Constitutive modelling of orthotropic plasticity in sheet metals. J. Mech. Phys. Solids 38, 405–417. https://doi.org/10.1016/0022-5096(90)90006-P.
Hou, Y., Du, K., Abd El-Aty, A., Lee, M.-G., Min, J., 2022a. Plastic anisotropy of sheet metals under plane strain loading: a novel non-associated constitutive model based on fourth-order polynomial functions. Mater. Des. 223, 111187. https://doi.org/10.1016/j.matdes.2022.111187.
Hou, Y., Du, K., Min, J., Lee, H.-R., Lou, Y., Park, N., Lee, M.-G., 2023a. A generalized, computationally versatile plasticity model framework - part I: theory and verification focusing on tension−compression asymmetry. Int. J. Plast., 103818 https://doi.org/10.1016/j.ijplas.2023.103818.
Hou, Y., Min, J., El-Aty, A.A., Han, H.N., Lee, M.-G., 2023b. A new anisotropic-asymmetric yield criterion covering wider stress states in sheet metal forming. Int. J. Plast. 166, 103653. https://doi.org/10.1016/j.ijplas.2023.103653.
Hou, Y., Min, J., Guo, N., Lin, J., Carsley, J.E., Stoughton, T.B., Traphöner, H., Clausmeyer, T., Tekkaya, A.E., 2021. Investigation of evolving yield surfaces of dual-phase steels. J. Mater. Process. Technol. 287, 116314. https://doi.org/10.1016/j.jmatprotec.2019.116314.
Hou, Y., Min, J., Lee, M.-G., 2023c. Non-associated and non-quadratic characteristics in plastic anisotropy of automotive lightweight sheet metals. Autom. Innov. 6, 364–378. https://doi.org/10.1007/s42154-023-00232-5.
Hou, Y., Min, J., Lin, J., Carsley, J.E., Stoughton, T.B., 2018a. Cruciform specimen design for large plastic strain during biaxial tensile testing. In: Proceedings of the Journal of Physics: Conference Series. IOP Publishing, 012160. https://doi.org/10.1088/1742-6596/1063/1/012160.
Hou, Y., Min, J., Lin, J., Carsley, J.E., Stoughton, T.B., 2018b. Plastic instabilities in AA5754-O under various stress states. IOP Conf. Ser.: Mater. Sci. Eng. IOP Publishing 012050. https://doi.org/10.1088/1757-899X/418/1/012050.
Hou, Y., Min, J., Lin, J., Lee, M.-G., 2022b. Modeling stress anisotropy, strength differential, and anisotropic hardening by coupling quadratic and stress-invariant-based yield functions under non-associated flow rule. Mech. Mater. 174, 104458. https://doi.org/10.1016/j.mechmat.2022.104458.
Hou, Y., Min, J., Stoughton, T.B., Lin, J., Carsley, J.E., Carlson, B.E., 2020. A non-quadratic pressure-sensitive constitutive model under non-associated flow rule with anisotropic hardening: modeling and validation. Int. J. Plast. 135, 102808. https://doi.org/10.1016/j.ijplas.2020.102808.
Hu, Q., Li, X., Han, X., Chen, J., 2017a. A new shear and tension based ductile fracture criterion: modeling and validation. Eur. J. Mech.-A/Solids 66, 370–386. https://doi.org/10.1016/j.ijmecsci.2018.09.004.
Hu, Q., Li, X., Han, X., Li, H., Chen, J., 2017b. A normalized stress invariant-based yield criterion: modeling and validation. Int. J. Plast. 99, 248–273. https://doi.org/10.1016/j.ijplas.2017.09.010.
Hu, Q., Maier, L., Nishiwaki, T., Hartmann, C., Volk, W., Yoon, J.W., 2024. User friendly FE Formulation for anisotropic distortional hardening model based on non-associated flow plasticity and its application to springback prediction. Thin-Walled Struct., 112142 https://doi.org/10.1016/j.tws.2024.112142.
Hu, Q., Yoon, J.W., Chen, J., 2023. Analytically described polynomial yield criterion by considering both plane strain and pure shear states. Int. J. Plast. 162, 103514. https://doi.org/10.1016/j.ijplas.2022.103514.
Hu, Q., Yoon, J.W., Stoughton, T.B., 2021. Analytical determination of anisotropic parameters for Poly6 yield function. Int. J. Mech. Sci. 201, 106467. https://doi.org/10.1016/j.ijmecsci.2021.106467.

Lee, H.-R., Lee, M.-G., Park, N., 2023. Effect of evolutionary anisotropic hardening on the prediction of deformation and forming load in incremental sheet forming simulation. Thin-Walled Struct. 193, 111231. https://doi.org/10.1016/j.tws.2023.111231.
Lee, J.W., Lee, M.G., Barlat, F., 2012. Finite element modeling using homogeneous anisotropic hardening and application to spring-back prediction. Int. J. Plast. 29, 13–41. https://doi.org/10.1016/j.ijplas.2011.07.007.
Lee, M.-G., Kim, D., Kim, C., Wenner, M.L., Chung, K., 2005. Spring-back evaluation of automotive sheets based on isotropic–kinematic hardening laws and non-quadratic anisotropic yield functions part III: applications. Int. J. Plast. 21, 915–953. https://doi.org/10.1016/j.ijplas.2004.05.014.
Li, H., Hu, X., Yang, H., Li, L., 2016. Anisotropic and asymmetrical yielding and its distorted evolution: modeling and applications. Int. J. Plast. 82, 127–158. https://doi.org/10.1016/j.ijplas.2016.03.002.
Li, W.T., Li, H., Fu, M.W., 2019. Interactive effect of stress state and grain size on fracture behaviours of copper in micro-scaled plastic deformation. Int. J. Plast. 114, 126–143. https://doi.org/10.1016/j.ijplas.2018.10.013.
Li, Z., Chang, Y., Liu, W., Lian, J., 2024. Predicting edge fracture in dual-phase steels: significance of anisotropy-induced localization. Int. J. Mech. Sci. 109255. https://doi.org/10.1016/j.ijmecsci.2024.109255.
Lian, J.H., Shen, F.H., Jia, X.X., Ahn, D.C., Chae, D.C., Munstermann, S., Bleck, W., 2018. An evolving non-associated Hill48 plasticity model accounting for anisotropic hardening and r-value evolution and its application to forming limit prediction. Int. J. Solids Struct. 151, 20–44. https://doi.org/10.1016/j.ijsolstr.2017.04.007.
Liu, W., Huang, J., Pang, Y., Zhu, K., Li, S., Ma, J., 2023a. Multi-scale modelling of evolving plastic anisotropy during Al-alloy sheet forming. Int. J. Mech. Sci. 247, 108168. https://doi.org/10.1016/j.ijmecsci.2023.108168.
Liu, X., He, J., Huang, S., 2023b. Mechanistically informed artificial neural network model for discovering anisotropic path-dependent plasticity of metals. Mater. Des., 111697 https://doi.org/10.1016/j.matdes.2023.111697.
Lou, Y., Huh, H., Yoon, J.W., 2013. Consideration of strength differential effect in sheet metals with symmetric yield functions. Int. J. Mech. Sci. 66, 214–223. https://doi.org/10.1016/j.ijmecsci.2012.11.010.
Lou, Y., Zhang, C., Wu, P., Whan Yoon, J., 2024. New geometry-inspired numerical convex analysis method for yield functions under isotropic and anisotropic hardenings. Int. J. Solids Struct. 112582. https://doi.org/10.1016/j.ijsolstr.2023.112582.
Lou, Y., Zhang, C., Zhang, S., Yoon, J.W., 2022. A general yield function with differential and anisotropic hardening for strength modelling under various stress states with non-associated flow rule. Int. J. Plast. 158, 103414. https://doi.org/10.1016/j.ijplas.2022.103414.
Lou, Y., Zhang, S., Yoon, J.W., 2020. Strength modeling of sheet metals from shear to plane strain tension. Int. J. Plast. 134, 102813. https://doi.org/10.1016/j.ijplas.2020.102813.
Meyer, K.A., Ekh, M., Ahlström, J., 2020. Anisotropic yield surfaces after large shear deformations in pearlitic steel. Eur. J. Mech.-A/Solids, 103977. https://doi.org/10.1016/j.euromechsol.2020.103977.
Min, J., Carsley, J.E., Lin, J., Wen, Y., Kuhlenkotter, B., 2016. A non-quadratic constitutive model under non-associated flow rule of sheet metals with anisotropic hardening: modeling and experimental validation. Int. J. Mech. Sci. 119, 343–359. https://doi.org/10.1016/j.ijmecsci.2016.10.027.
Min, J., Guo, N., Hou, Y., Jiang, K., Chen, X., Carsley, J.E., Lin, J., 2021. Effect of tension-compression testing strategy on kinematic model calibration and springback simulation of advanced high strength steels. Int. J. Mater. Form. 14, 435–448. https://doi.org/10.1007/s12289-020-01583-8.
Min, J., Kong, J., Hou, Y., Liu, Z., Lin, J., 2022. Application of laser deposition to mechanical characterization of advanced high strength steels subject to non-proportional loading. Exp. Mech. 62, 685–700. https://doi.org/10.1007/s11340-022-00820-2.
Mirnia, M.J., Vahdani, M., 2020. Calibration of ductile fracture criterion from shear to equibiaxial tension using hydraulic bulge test. J. Mater. Process. Technol. 280, 116589. https://doi.org/10.1016/j.jmatprotec.2020.116589.
Mu, Z., Liu, J., Wang, W., Dai, X., Ma, S., Hou, Y., 2024. Characterization and modeling of biaxial plastic anisotropy in metallic sheets. Int. J. Mech. Sci. 282, 109640. https://doi.org/10.1016/j.ijmecsci.2024.109640.
Mu, Z., Wang, W., Zhang, S., Zheng, Z., Yan, H., Liu, S., Ma, S., Du, K., Hou, Y., 2024. Towards improved description of plastic anisotropy in sheet metals under biaxial loading: A novel generalization of Hill48 yield criterion. Mater. Today Commun. 41, 110222. https://doi.org/10.1016/j.mtcomm.2024.110222.
Park, J., Hou, Y., Min, J., Hou, Z., Han, H.N., He, B., Lee, M.-G., 2024. Understanding plasticity in multiphase quenching & partitioning steels: insights from crystal plasticity with stress state-dependent martensitic transformation. Int. J. Plast. 104075. https://doi.org/10.1016/j.ijplas.2024.104075.
Peirs, J., Verleysen, P., Degrieck, J., 2012. Novel technique for static and dynamic shear testing of Ti6Al4V Sheet. Exp. Mech. 52, 729–741. https://doi.org/10.1007/s11340-011-9541-9.
Raemy, C., Manopulo, N., Hora, P., 2017. On the modelling of plastic anisotropy, asymmetry and directional hardening of commercially pure titanium: a planar Fourier series based approach. Int. J. Plast. 91, 182–204. https://doi.org/10.1016/j.ijplas.2017.02.010.
Raemy, C., Manopulo, N., Hora, P., 2018. A generalized anisotropic and asymmetric yield criterion with adjustable complexity. C.R. Mec. 346, 779–793. https://doi.org/10.1016/j.crme.2018.05.002.
Rahmaan, T., Noder, J., Abedini, A., Zhou, P., Butcher, C., Worswick, M.J., 2020. Anisotropic plasticity characterization of 6000-and 7000-series aluminum sheet alloys at various strain rates. Int. J. Impact Eng. 103390. https://doi.org/10.1016/j.ijimpeng.2019.103390.
Rong, H., Ying, L., Hu, P., Hou, W., 2021. Characterization on the thermal anisotropic behaviors of high strength AA7075 alloy with the Yld2004-18p yield function. J. Alloys Compd. 877, 159955. https://doi.org/10.1016/j.jallcom.2021.159955.
Rousselier, G., 2022. Lode-dependent second porosity in porous plasticity for shear-dominated loadings. Int. J. Plast. 103446. https://doi.org/10.1016/j.ijplas.2022.103446.
Sato, S., Kim, M., Ha, J., Korkolis, Y.P., Kuwabara, T., 2023. Cruciform tension-shear test for sheet metal: evaluation of methods for calculating plastic work. IOP Conf. Ser.: Mater. Sci. Eng. 1284, 012074. https://doi.org/10.1088/1757-899X/1284/1/012074.
Scherzinger, W.M., 2017. A return mapping algorithm for isotropic and anisotropic plasticity models using a line search method. Comput. Methods Appl. Mech. Eng. 317, 526–553. https://doi.org/10.1016/j.cma.2016.11.026.
Shang, X., Zhang, H., Wang, L., Zhu, G., Cui, Z., Fu, M.W., Zeng, X., 2021. The effect of stress state and strain partition mode on the damage behavior of a Mg-Ca alloy. Int. J. Plast. 103040. https://doi.org/10.1016/j.ijplas.2021.103040.
Shen, F., Sparrer, Y., Rao, J., Könemann, M., Münstermann, S., Lian, J., 2024. A forming limit framework accounting for various failure mechanisms: localization, ductile and cleavage fracture. Int. J. Plast. 175, 103921. https://doi.org/10.1016/j.ijplas.2024.103921.
Stoughton, T.B., 2002. A non-associated flow rule for sheet metal forming. Int. J. Plast. 18, 687–714. https://doi.org/10.1016/S0749-6419(01)00053-5.
Stoughton, T.B., Yoon, J.W., 2004. A pressure-sensitive yield criterion under a non-associated flow rule for sheet metal forming. Int. J. Plast. 20, 705–731. https://doi.org/10.1016/S0749-6419(03)00079-2.
Traphöner, H., Clausmeyer, T., Tekkaya, A.E., 2021. Methods for measuring large shear strains in in-plane torsion tests. J. Mater. Process. Technol. 287, 116516. https://doi.org/10.1016/j.jmatprotec.2019.116516.
Vegter, H., Boogaard, A.H.v.d., 2006. A plane stress yield function for anisotropic sheet material by interpolation of biaxial stress states. Int. J. Plast. 22, 557–580. https://doi.org/10.1016/j.ijplas.2005.04.009.
Wu, K., Zhang, S., Weiss, M., Yoon, J.W., 2024. Modeling of distortional hardening including plane strain tension and pure shear for a TWIP steel. Int. J. Mater. Form. 17, 37. https://doi.org/10.1007/s12289-024-01835-x.
Yoon, J.W., Barlat, F., Gracio, J.J., Rauch, E., 2005. Anisotropic strain hardening behavior in simple shear for cube textured aluminum alloy sheets. Int. J. Plast. 21, 2426–2447. https://doi.org/10.1016/j.ijplas.2005.03.014.
Yoon, J.W., Lou, Y.S., Yoon, J., Glazoff, M.V., 2014. Asymmetric yield function based on the stress invariants for pressure sensitive metals. Int. J. Plast. 56, 184–202. https://doi.org/10.1016/j.ijplas.2013.11.008.
Yoshida, F., Hamasaki, H., Uemori, T., 2013. A user-friendly 3D yield function to describe anisotropy of steel sheets. Int. J. Plast. 45, 119–139. https://doi.org/10.1016/j.ijplas.2013.01.010.

Zhang, C., Lou, Y., 2023. Characterization and modelling of evolving plasticity behaviour up to fracture for FCC and BCC metals. J. Mater. Process. Technol., 117997 https://doi.org/10.1016/j.jmatprotec.2023.117997.

Zhang, C., Lou, Y., 2024. Influences of the evolving plastic behavior of sheet metal on V-bending and springback analysis considering different stress states. Int. J. Plast., 103889 https://doi.org/10.1016/j.ijplas.2024.103889.

Zhang, C., Zhang, S., Lou, Y., 2022a. Characterization of kinematic and distortional hardening by cyclic twin-bridge shear tests for sheet metal with inverse engineering approach. Mech. Mater., 104387 https://doi.org/10.1016/j.mechmat.2022.104387.

Zhang, Y., Van Bael, A., Andrade-Campos, A., Coppieters, S., 2022b. Parameter identifiability analysis: mitigating the non-uniqueness issue in the inverse identification of an anisotropic yield function. Int. J. Solids Struct. 243, 111543. https://doi.org/10.1016/j.ijsolstr.2022.111543.

Zheng, L., Wang, Z., Meng, B., Wan, M., 2023. A unified ductile fracture criterion suitable for sheet and bulk metals considering multiple void deformation modes. Int. J. Plast. 164, 103572. https://doi.org/10.1016/j.ijplas.2023.103572.

Zheng, L., Yoon, J.W., 2024. A flexible yield criterion for strength modeling from biaxial compression to biaxial tension. Int. J. Plast. 182, 104113. https://doi.org/10.1016/j.ijplas.2024.104113.

Zhou, Y., Hu, Q., Chen, J., 2023. A concise analytical framework for describing asymmetric yield behavior based on the concept of shape functions. Int. J. Plast., 103593 https://doi.org/10.1016/j.ijplas.2023.103593.